



AR-008-995

DSTO-RR-0020

Calculations of the Sound Scattering  
from Fluid-filled Spherical Shell  
Sonar Targets

Mark Readhead

19951108 096

Approved for Public Release

DTIC QUALITY INSPECTED 5

© Commonwealth of Australia

THE UNITED STATES NATIONAL  
TECHNICAL INFORMATION SERVICE  
IS AUTHORISED TO  
REPRODUCE AND SELL THIS REPORT

# Calculations of the Sound Scattering from Fluid-Filled Spherical Shell Sonar Targets

*Mark Readhead*

**Maritime Operations Division  
Aeronautical and Maritime Research Laboratory**

DSTO-RR-0020

## ABSTRACT

The theory of the sound pressure scattered from a fluid-filled spherical shell immersed in a second fluid is developed. An arbitrary combination of fluids may be used to fill the shell, and both the sound source and the receiver may be in the near field. The theory is used to calculate the pressure field in both the interior and exterior fluids and is extended to determine the time-dependence of the reflected signal and the target strength. The dependence of these quantities as a function of frequency and pulse type; shell material, diameter and wall thickness; fluid combination; temperature; and distance of the receiver from the sphere is examined, and is shown to be sensitive to most of these parameters. The performance of spheres filled with a Freon-113<sup>TM</sup> - ethanol or Fluorinert FC-72<sup>TM</sup> - n-hexane mixture is considered.

Approved for public release  
This document contains neither recommendations nor conclusions of the Defense Science and Technology Organization. It has been approved for public release by the Defense Science and Technology Organization. It contains neither recommendations nor conclusions of the Defense Science and Technology Organization. It is the property of the Defense Science and Technology Organization, is not to be distributed outside your organization, and is to be controlled in accordance with the instructions on the reverse side of this page.

## RELEASE LIMITATION

*Approved for public release*

DEPARTMENT OF DEFENCE

DEFENCE SCIENCE AND TECHNOLOGY ORGANISATION

Accession For	
ETIS GRA&I	<input checked="" type="checkbox"/>
DTIC TAB	<input type="checkbox"/>
Unannounced	<input type="checkbox"/>
Justification	
By _____	
Distribution/	
Availability Codes	
Dist	Avail and/or
	Special
A-1	

*Published by*

*DSTO Aeronautical and Maritime Research Laboratory  
PO Box 4331  
Melbourne Victoria 3001*

*Telephone: (03) 626 8111  
Fax: (03) 626 8999  
© Commonwealth of Australia 1995  
AR No. 008-995  
January 1995*

**APPROVED FOR PUBLIC RELEASE**

# Calculations of the Sound Scattering from Fluid-Filled Spherical Shell Sonar Targets

## Executive Summary

The theory of the sound pressure scattered from a fluid-filled spherical shell immersed in a second fluid is developed. The prime reason for developing the theory is to aid in the design of fluid-filled spheres of known target strength, the target strength being a measure of the reflected intensity. An arbitrary combination of fluids may be used to fill the shell, and both the sound source and the receiver may be placed near to or far from the sphere. The theory is used to calculate the pressure field in both the interior and exterior fluids and is extended to determine the time-dependence and intensity of the reflected signal.

Not only is the target strength found to be sensitive to a number of material parameters, but with a given selection of materials, it is also sensitive to both the form of the incoming sound waves and the environment. The target strength varies greatly for small changes in the frequency if continuous waves are used. Fortunately, these variations can be largely eliminated by the use of pulsed signals, which effectively average over many frequencies.

A shell of aluminium or pyrex glass optimises the target strength, but as these are soft or brittle materials, stainless steel might be preferable as it is more robust. As might be expected, increasing the diameter of the sphere will give a larger target strength. A thin shell wall will also lead to a large target strength, but may be too difficult to manufacture and will be easily damaged. A thickness of 0.8 mm might be classed as a reasonable compromise. The target strength is quite sensitive to the thickness, so variations in the wall thickness need to be avoided in the manufacturing.

Choice of the optimum combination of fluids with which to fill the shell depends on the temperature. Variations of a few degrees will make only a modest change to the target strength, but a combination chosen for warm waters will behave quite differently in cool waters. For frequencies below 200 kHz a mixture of Freon-113™ and ethanol, or Fluorinert FC-72™ and n-hexane will work quite well if the ratio of liquids is chosen to give a refractive index between 1.8 and 1.9. At frequencies above 250 kHz the same liquids mixed to give a refractive index between 1.6 and 1.7 will produce high target strengths.

## Author

### **Mark Readhead** Maritime Operations Division



*Mark Readhead obtained a BSc(Hons) in Physics from the University of Western Australia in 1979, and a PhD in Physics from the Australian National University in 1984. After lecturing in Physics and holding the position of Postdoctoral Research Associate at the University of Washington, he joined DSTO in 1989. He works with the sonar group of the Maritime Operations Division and current research interests include the performance of fluid-filled spherical shells, target strengths of sea mines, absorption of sound by sea water, and the distribution of underwater noise sources.*

---

## Contents

1. INTRODUCTION .....	1
2. THEORY .....	1
2.1 Continuous Waves .....	1
2.2 Pulsed Signals .....	9
2.2.1 Tone Bursts .....	9
2.2.2 Chirps .....	10
2.3 Binary Fluids .....	12
3. PHYSICAL DATA .....	12
4. COMPUTATIONAL CONSIDERATIONS .....	16
5. RESULTS .....	17
6. CONCLUSIONS .....	52
7. REFERENCES .....	66
APPENDIX A .....	68
APPENDIX B .....	72
APPENDIX C .....	74
APPENDIX D .....	76
APPENDIX E .....	80

## 1. Introduction

For the calibration of sonar systems, spherical targets are advantageous in that they are aspect independent. That is, they scatter the same intensity of sound into a particular direction, regardless of the target's orientation. However, a major limitation is that a solid sphere or air-filled spherical shell is usually a weak scatterer in comparison to non-aspect independent reflectors made up of multiple corner reflectors. An attractive alternative, providing both aspect independence and strong scattering, is a fluid-filled spherical shell in which the filling fluid is chosen so as to cause focusing of the reflected sound in the backscatter direction. This direction is important experimentally.

This study considers such sonar targets and the effect the various parameters have on their performance. The aim is to enable selection of appropriate materials and to show how the performance of the target alters with small changes in the material or environmental parameters.

The scattering of sound from spherical objects has been the subject of some investigation in the past. Rayleigh (1945) considered the limiting case where the scatterer was small compared to the wavelength. Morse (1936) derived a solution for rigid immovable spheres, which were not necessarily small compared to the wavelength. Faran (1951) allowed penetration of sound into solid spheres; Junger (1952) considered the scattering by thin hollow elastic shells. Goodman and Stern (1962) also considered elastic spherical shells, but with the internal and external fluids the same. Hickling (1964) analysed evacuated metal spheres in water.

Apart from restrictions on the interior fluid, in each of these studies it was assumed that the sphere was in the far field of the projector. However, the theory enabling the scattered sound pressure to be calculated will be developed in the following section without these limitations, by solving the wave equation for a fluid-filled spherical shell immersed in another fluid. A point source of sound waves and a point isotropic receiver are located in the external fluid. The former may be arbitrarily placed, but the receiver must be no further away from the centre of the sphere than the projector.

## 2. Theory

### 2.1 Continuous Waves

Consider a fluid medium of infinite extent whose density is  $\rho_1$  and which supports longitudinal sound waves of speed  $c_1$ . In the medium is a fluid-filled spherical shell, with its centre located at the origin of the spherical coordinate system, as shown in Fig. 1. The inner and outer radii of the shell are  $a$  and  $b$ , respectively. The shell has a density  $\rho_2$  and supports both longitudinal and transverse waves of velocity  $c_{L,2}$  and  $c_{T,2}$ , respectively. The interior fluid has a density  $\rho_3$  and a longitudinal sound speed of  $c_3$ . Located at  $r = r_p$  and  $\theta = 0$  with respect to the origin is a point source of

continuous sinusoidal sound waves. The incident pressure a distance  $R$  away in the external fluid is

$$P_i = P_0 \frac{e^{i(2\pi f t - k_{L,1} R)}}{R} \quad (1)$$

where  $P_0$  is the amplitude of the pressure wave 1 m from the source,  $f$  is the frequency of the wave and  $k_{L,1}$  is the wavenumber in the fluid.  $k_{L,1}$  is related to  $f$  by

$$k_{L,1} = \frac{2\pi f}{c_1}. \quad (2)$$

The displacement component of the incident pressure can be written as

$$p_i = P_0 \frac{e^{-ik_{L,1} R}}{R}. \quad (3)$$

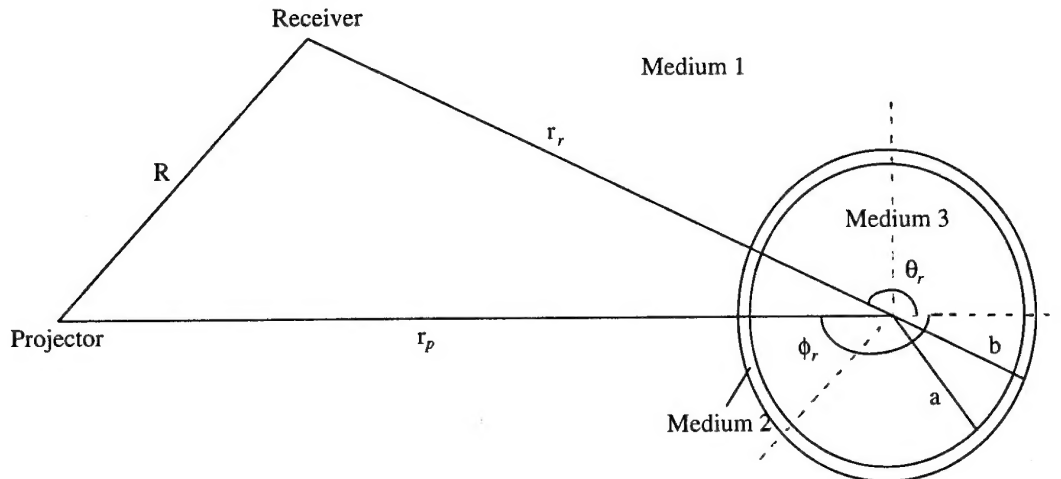


Figure 1: Geometry for projector, receiver and fluid-filled sphere.

When the sound waves strike the sphere, some of the sound will be transmitted into the shell and the filling fluid, and some will be scattered back into the exterior medium. The prime focus of this study will be to derive the scattered pressure at the listening point of  $r = r_r$  and  $\theta = \theta_r$ . This can be found by satisfying the boundary conditions at the surfaces of the shell. For a fluid and shell behaving in a linear fashion, a shell of zero viscosity and with no cavitation occurring, these are:

- i) the pressure in the fluid must be equal to the normal component of stress in the shell at the interfaces,

- ii) the normal (radial) component of displacement of the fluid must be equal to the normal component of displacement of the shell at the interfaces, and
- iii) the tangential components of shearing stress must vanish at the surfaces of the shell.

Symbolically,

$$\left. \begin{array}{l} p_1 = -[rr] \\ u_{r,1} = u_{r,2} \\ [r\theta] = [r\phi] = 0 \end{array} \right\} \text{at } r = b \quad \left. \begin{array}{l} p_3 = -[rr] \\ u_{r,3} = u_{r,2} \\ [r\theta] = [r\phi] = 0 \end{array} \right\} \text{at } r = a \quad (4)$$

where the  $p_1$  and  $p_3$  are the pressures in the external and internal fluids, with the former being the sum of the incident and scattered pressures

$$p_1 = p_i + p_s. \quad (5)$$

The  $u_r$  are the radial components of the displacement in the various media and  $[rr]$ ,  $[r\theta]$  and  $[r\phi]$  are the radial and tangential components of the stress in the shell.

The pressures in the fluids can be found by solving

$$\nabla^2 P = \frac{1}{c_{L,i}^2} \frac{\partial^2 P}{\partial t^2} \quad (6)$$

in which  $i$  is 1 or 3. This is done in Appendix A using the spherical coordinate system, separating out the time and position variables and noting that  $P$  has no  $\phi$  dependence, to yield

$$P = p(r, \theta).T(t) \quad (7)$$

where in the external and internal fluids  $p(r, \theta)$  is

$$p_1 = \sum_{l=0}^{\infty} P_l(\cos \theta_r) A_l h_l(k_{L,1} r_r) \quad (8)$$

and

$$p_3 = \sum_{l=0}^{\infty} P_l(\cos \theta_r) B_l j_l(k_{L,3} r_r) \quad (9)$$

respectively.  $h_l$  and  $j_l$  are the spherical Hankel and Bessel functions of order  $l$ ;  $P_l$  is the Legendre function of order  $l$ .

It will be more convenient to use different summations at a later stage. Using a series expansion given by Morse and Feshbach (1953, p. 1574), the incident pressure in equation (3) can be written as

$$p_i = -iP_0 k_{L,1} \sum_{l=0}^{\infty} (-1)^l (2l+1) h_l^*(k_{L,1} r_p) j_l(k_{L,1} r_r) P_l(\cos \theta_r) \quad \text{for } 0 < r_r < r_p \quad (10)$$

where the listening point is at  $r = r_r$  and  $\theta = \theta_r$  with respect to the origin, and  $R$ ,  $r_p$ ,  $r_r$  and  $\theta_r$  are related by the cosine rule:

$$R^2 = r_r^2 + r_p^2 - 2r_r r_p \cos \theta_r. \quad (11)$$

Using an expression of Morse and Ingard (1968, p. 419) it can be shown that at the listening point of  $r = r_r$  and  $\theta = \theta_r$ , the scattered pressure will be

$$p_s = P_0 k_{L,1} \sum_{l=0}^{\infty} (-1)^l (2l+1) C_l h_l^*(k_{L,1} r_p) h_l^*(k_{L,1} r_r) P_l(\cos \theta_r) \quad \text{for } 0 < r_r < r_p \quad (12)$$

where the  $C_l$  are coefficients to be determined. Once these coefficients have been obtained, the scattered pressure will be known, which is the main focus of this study. The pressure in the external fluid, as given in equation (5), is found by summing equations (10) and (12). The pressure in the internal fluid is of the same form as in equation (10), namely

$$p_3 = -iP_0 k_{L,3} \sum_{l=0}^{\infty} (-1)^l (2l+1) D_l h_l^*(k_{L,3} r_p) j_l(k_{L,3} r_r) P_l(\cos \theta_r) \quad \text{for } 0 < r_r < r_p \quad (13)$$

where the  $D_l$  are coefficients to be determined.

The radial displacements in the fluids are found by using

$$\vec{u} = \frac{1}{4\pi^2 f^2 \rho} \vec{\nabla} p \quad (14)$$

to yield

$$u_{r,1} = \frac{1}{4\pi^2 f^2 \rho_1} \frac{\partial p_1}{\partial r} \quad (15)$$

$$= \frac{k_{L,1}^2 P_0}{4\pi^2 f^2 \rho_1} \sum_{l=0}^{\infty} (-1)^l (2l+1) P_l(\cos \theta_r) h_l^*(k_{L,1} r_p) \left[ -i \frac{\partial}{\partial x} j_l(x) + C_l \frac{\partial}{\partial x} h_l^*(x) \right] \quad (16)$$

and

$$u_{r,3} = \frac{1}{4\pi^2 f^2 \rho_3} \frac{\partial p_3}{\partial r} \quad (17)$$

$$= \frac{-ik_{L,3}^2 P_0}{4\pi^2 f^2 \rho_3} \sum_{l=0}^{\infty} (-1)^l (2l+1) P_l(\cos \theta_r) h_l^*(k_{L,3} r_p) D_l \frac{\partial}{\partial y} j_l(y) \quad (18)$$

for the external and internal fluids respectively, where  $x = k_{L,1} r$ , and  $y = k_{L,3} r$ .

To find the displacements and stresses in the shell requires the solution of the wave equation,

$$c_{L,2}^2 \vec{\nabla}(\vec{\nabla} \cdot \vec{u}) - c_T^2 \vec{\nabla} \times \vec{\nabla} \times \vec{u} = \frac{\partial^2 \vec{u}}{\partial t^2}. \quad (19)$$

The displacement is derived from a scalar and vector potential.

$$\vec{u} = -\vec{\nabla} \Psi + \vec{\nabla} \times \vec{A} \quad (20)$$

where

$$\nabla^2 \Psi = \frac{1}{c_{L,2}^2} \frac{\partial^2 \Psi}{\partial t^2} \quad (21)$$

and

$$-\vec{\nabla} \times \vec{\nabla} \times \vec{A} = \frac{1}{c_T^2} \frac{\partial^2 \vec{A}}{\partial t^2}. \quad (22)$$

Equation (21) is of the same form as equation (6), and can be solved as in Appendix A to give

$$\Psi = \psi(r, \theta) T(t) \quad (23)$$

where

$$\psi = \sum_{l=0}^{\infty} P_l(\cos \theta_r) [E_l j_l(k_{L,2} r_r) + F_l n_l(k_{L,2} r_r)]. \quad (24)$$

$n_l$  is the spherical Neumann function of order  $l$ . Again using the spherical coordinate system, separating out the time and position variables and noting that  $\vec{A} = (0, 0, A_\phi)$ , equation (22) can be solved (see Appendix B) to yield

$$A_\phi = \alpha_\phi(r, \theta, \phi) T(t) \quad (25)$$

where

$$\alpha_\phi = \sum_{l=0}^{\infty} \frac{\partial}{\partial \theta} P_l(\cos \theta_r) [G_l j_l(k_T r_r) + H_l n_l(k_T r_r)]. \quad (26)$$

Returning to equation (20), the displacements in the shell are

$$u_{r,2} = -\frac{\partial \Psi}{\partial r} + \frac{1}{r^2 \sin \theta} \frac{\partial}{\partial \theta} (r \alpha_\phi \sin \theta) \quad (27)$$

$$= \sum_{l=0}^{\infty} -P_l(\cos \theta_r) \left\{ \frac{l(l+1)}{r_r} [G_l j_l(k_T r_r) + H_l n_l(k_T r_r)] + k_{L,2} \left[ E_l \frac{\partial}{\partial z} j_l(z) + F_l \frac{\partial}{\partial z} n_l(z) \right] \right\} \quad (28)$$

$$u_{\theta,2} = -\frac{1}{r} \frac{\partial \Psi}{\partial \theta} + \frac{1}{r \sin \theta} \frac{\partial}{\partial r} (r \alpha_\phi \sin \theta) \quad (29)$$

$$\begin{aligned} &= \sum_{l=0}^{\infty} \frac{\partial P_l(\eta)}{\partial \eta} \sin \theta \left\{ \frac{1}{r_r} [E_l j_l(k_{L,2} r_r) + F_l n_l(k_{L,2} r_r)] + \frac{1}{r_r} [G_l j_l(k_T r_r) + H_l n_l(k_T r_r)] \right. \\ &\quad \left. + k_T \left[ G_l \frac{\partial}{\partial \tau} j_l(\tau) + H_l \frac{\partial}{\partial \tau} n_l(\tau) \right] \right\} \end{aligned} \quad (30)$$

and

$$u_{\phi,2} = 0 \quad (31)$$

where  $\eta = \cos \theta_r$ ,  $z = k_{L,2} r_r$ , and  $\tau = k_T r_r$ .

The stresses in the shell are (Faran, 1951)

$$[r r] = 2\rho_2 c_{T,2}^2 \left[ \frac{\sigma}{1-2\sigma} \vec{\nabla} \cdot \vec{u} + \frac{\partial u_{r,2}}{\partial r} \right] \quad (32)$$

$$[r \theta] = \mu \left[ \frac{\partial u_{\theta,2}}{\partial r} - \frac{u_{\theta,2}}{r} + \frac{1}{r} \frac{\partial u_{r,2}}{\partial \theta} \right] \quad (33)$$

$$[r \phi] = \mu \left[ \frac{1}{r \sin \theta} \frac{\partial u_{r,2}}{\partial \theta} + \frac{\partial u_{\phi,2}}{\partial r} - \frac{u_{\phi,2}}{r} \right] \quad (34)$$

where  $\sigma$  and  $\mu$  are Poisson's ratio and the Lamé elastic constant of the shell material, respectively. Using

$$\vec{\nabla} \cdot \vec{u} = \frac{1}{r^2} \frac{\partial}{\partial r} (r^2 u_{r,2}) + \frac{1}{r \sin \theta} \frac{\partial}{\partial \theta} (\sin \theta \cdot u_{\theta,2}) + \frac{1}{r \sin \theta} \frac{\partial u_\phi}{\partial \phi} \quad (35)$$

$$= \sum_{l=0}^{\infty} P_l(\cos \theta_r) k_{L,2}^2 [E_l j_l(k_{L,2} r_r) + F_l n_l(k_{L,2} r_r)] \quad (36)$$

these become

$$[r \ r] = 2 \rho_2 c_{T,2}^2 \sum_{l=0}^{\infty} P_l(\cos \theta_r) \left\{ \frac{\sigma}{1-2\sigma} k_{L,2}^2 [E_l j_l(k_{L,2} r_r) + F_l n_l(k_{L,2} r_r)] - k_{L,2}^2 \left[ E_l \frac{\partial^2}{\partial z^2} j_l(z) + F_l \frac{\partial^2}{\partial z^2} n_l(z) \right] \right. \\ \left. + \frac{l(l+1)}{r_r^2} [G_l j_l(k_T r_r) + H_l n_l(k_T r_r)] - \frac{l(l+1)}{r_r} k_T \left[ G_l \frac{\partial}{\partial \tau} j_l(\tau) + H_l \frac{\partial}{\partial \tau} n_l(\tau) \right] \right\} \quad (37)$$

$$[r \ \theta] = \mu \sum_{l=0}^{\infty} \frac{\partial P_l(\eta)}{\partial \eta} \sin \theta_r \left\{ -\frac{2}{r_r^2} [E_l j_l(k_{L,2} r_r) + F_l n_l(k_{L,2} r_r)] + \frac{2 k_{L,2}}{r_r} \left[ E_l \frac{\partial}{\partial z} j_l(z) + F_l \frac{\partial}{\partial z} n_l(z) \right] \right. \\ \left. + \frac{l(l+1)-2}{r_r^2} [G_l j_l(k_T r_r) + H_l n_l(k_T r_r)] + k_T^2 \left[ G_l \frac{\partial^2}{\partial \tau^2} j_l(\tau) + H_l \frac{\partial^2}{\partial \tau^2} n_l(\tau) \right] \right\} \quad (38)$$

and

$$[r \ \phi] = \mu \sum_{l=0}^{\infty} \frac{1}{r_r} \frac{\partial P_l(\eta)}{\partial \eta} \left\{ \frac{l(l+1)}{r_r} [G_l j_l(k_T r_r) + H_l n_l(k_T r_r)] + k_{L,2} \left[ E_l \frac{\partial}{\partial z} j_l(z) + F_l \frac{\partial}{\partial z} n_l(z) \right] \right\} \quad (39)$$

Substitution of equations (5), (10), (12), (13), (16), (18), (28), (30), (37), (38) and (39) into equation (4) and evaluation at  $r=a$  and  $r=b$  yields eight simultaneous equations from which the coefficients  $C_l$  needed to evaluate the scattered pressure can be determined. After some simplification these are given by

$$C_l = -i \frac{\begin{vmatrix} \gamma_{11} & \gamma_{12} & \gamma_{13} & \gamma_{14} & g_1 & 0 \\ \gamma_{21} & \gamma_{22} & \gamma_{23} & \gamma_{24} & 0 & \gamma_{26} \\ \gamma_{31} & \gamma_{32} & \gamma_{33} & \gamma_{34} & g_3 & 0 \\ \gamma_{41} & \gamma_{42} & \gamma_{43} & \gamma_{44} & 0 & \gamma_{46} \\ \gamma_{51} & \gamma_{52} & \gamma_{53} & \gamma_{54} & 0 & 0 \\ \gamma_{61} & \gamma_{62} & \gamma_{63} & \gamma_{64} & 0 & 0 \end{vmatrix}}{\begin{vmatrix} \gamma_{11} & \gamma_{12} & \gamma_{13} & \gamma_{14} & \gamma_{15} & 0 \\ \gamma_{21} & \gamma_{22} & \gamma_{23} & \gamma_{24} & 0 & \gamma_{26} \\ \gamma_{31} & \gamma_{32} & \gamma_{33} & \gamma_{34} & \gamma_{35} & 0 \\ \gamma_{41} & \gamma_{42} & \gamma_{43} & \gamma_{44} & 0 & \gamma_{46} \\ \gamma_{51} & \gamma_{52} & \gamma_{53} & \gamma_{54} & 0 & 0 \\ \gamma_{61} & \gamma_{62} & \gamma_{63} & \gamma_{64} & 0 & 0 \end{vmatrix}}. \quad (40)$$

The coefficients required to evaluate equation (40) are listed in Appendix C. The coefficients  $D_l$  needed to calculate the pressure in the filling fluid are given by

$$D_l = -\frac{k_{L,1}h_l^*(k_{L,1}r_p)}{k_{L,3}h_l^*(k_{L,3}r_p)} \frac{\begin{vmatrix} \gamma_{11} & \gamma_{12} & \gamma_{13} & \gamma_{14} & \gamma_{15} & g_1 \\ \gamma_{21} & \gamma_{22} & \gamma_{23} & \gamma_{24} & 0 & 0 \\ \gamma_{31} & \gamma_{32} & \gamma_{33} & \gamma_{34} & \gamma_{35} & g_3 \\ \gamma_{41} & \gamma_{42} & \gamma_{43} & \gamma_{44} & 0 & 0 \\ \gamma_{51} & \gamma_{52} & \gamma_{53} & \gamma_{54} & 0 & 0 \\ \gamma_{61} & \gamma_{62} & \gamma_{63} & \gamma_{64} & 0 & 0 \end{vmatrix}}{\begin{vmatrix} \gamma_{11} & \gamma_{12} & \gamma_{13} & \gamma_{14} & \gamma_{15} & 0 \\ \gamma_{21} & \gamma_{22} & \gamma_{23} & \gamma_{24} & 0 & \gamma_{26} \\ \gamma_{31} & \gamma_{32} & \gamma_{33} & \gamma_{34} & \gamma_{35} & 0 \\ \gamma_{41} & \gamma_{42} & \gamma_{43} & \gamma_{44} & 0 & \gamma_{46} \\ \gamma_{51} & \gamma_{52} & \gamma_{53} & \gamma_{54} & 0 & 0 \\ \gamma_{61} & \gamma_{62} & \gamma_{63} & \gamma_{64} & 0 & 0 \end{vmatrix}}. \quad (41)$$

where the elements of the determinants are again as listed in Appendix C.

Inserting the coefficients of equation (40) into equation (12) yields the scattered pressure at the listening point of  $r = r_r$  and  $\theta = \theta_r$ . A convenient way of presenting this pressure is to relate it to that incident upon the sphere, in the form

$$20 \log \left( \left| r_p r_r \frac{p_s|_{r=r_r}}{P_0} \right| \right). \quad (42)$$

If  $\theta = 180^\circ$  and  $r_r$  is sufficiently large so that spherical spreading applies, i.e. in the far-field, then this term equals the backscatter target strength, defined by

$$TS = 20 \log \left( \left| \frac{p_s|_{\theta=180^\circ, r=1}}{p_i} \right| \right) \quad (43)$$

where the scattered pressure is evaluated 1 m from the centre of the sphere along the axis to the source. In the comparisons reported below, the scattered pressure will be given as the target strength via expression (42) with  $\theta = 180^\circ$  and both  $r_p$  and  $r_r$  generally set to 1000 m to ensure equivalence with equation (43).

## 2.2 Pulsed Signals

Until now the point source has been considered as producing continuous sinusoidal waves. However, in an experiment tone bursts or chirped signals are more likely to be used. The scattered pressure for these two cases will now be considered.

### 2.2.1 Tone Bursts

Consider first a tone burst of central frequency  $f_0$  and duration  $\Delta t$ . Defining

$$k_{L,1}^0 = \frac{2\pi f_0}{c_1} \quad (44)$$

and

$$\text{rect}(t) = \begin{cases} 1 & \text{for } -\frac{1}{2} \leq t \leq \frac{1}{2} \\ 0 & \text{elsewhere} \end{cases} \quad (45)$$

we have, from equation (1),

$$P_i(t) = \frac{P_0 e^{-ik_{L,1}^0 R}}{R} e^{i2\pi f_0 t} \text{rect}\left(\frac{1}{\Delta t} \left(t - \frac{R}{c}\right)\right) \quad (46)$$

which has the Fourier transform

$$P_i(f) = \int_{-\Delta t/2}^{\Delta t/2} \frac{P_0 e^{-ik_{L,1}^0 R}}{R} e^{i2\pi f_0 t} e^{-i2\pi f t} dt \quad (47)$$

$$= \frac{P_0 e^{-ik_{L,1}^0 R}}{R} \frac{\sin[\pi(f - f_0)\Delta t]}{\pi(f - f_0)} \quad (48)$$

as the frequency components. As this is the product of a continuous wave mono-frequency source and a weighting function, the scattered pressure frequency

components may be represented by the continuous wave solution multiplied by the same weighting function. Thus

$$P_s(f) = p_s(f) \frac{\sin[\pi(f-f_0)\Delta t]}{\pi(f-f_0)} \quad (49)$$

where  $p_s$  is given by equation (12). Applying the inverse Fourier transform, we obtain, as a function of time,

$$P_s(t) = \int_{-\infty}^{\infty} p_s(f) \frac{\sin[\pi(f-f_0)\Delta t]}{\pi(f-f_0)} e^{i2\pi ft} df. \quad (50)$$

## 2.2.2 Chirps

For a chirped signal of start frequency  $f_0$ , stop frequency  $f_1$ , central frequency  $f_c$  and duration  $\Delta t$ , equation (46) is altered to

$$P_i(t) = \frac{P_0 e^{-ik_{L1}R}}{R} e^{i2\pi \left[ f_c t + \frac{(f_1-f_0)}{2\Delta t} t^2 \right]} \text{rect}\left( \frac{1}{\Delta t} \left( t - \frac{R}{c} \right) \right) \quad (51)$$

where

$$k_{L1}^c = \frac{2\pi f_c}{c_1}. \quad (52)$$

The incident signal frequency components are

$$P_i(f) = \frac{P_0 e^{-ik_{L1}R}}{R} \int_{-\Delta t/2}^{\Delta t/2} e^{i2\pi \left[ (f_c - f)t + \frac{(f_1-f_0)}{2\Delta t} t^2 \right]} dt. \quad (53)$$

The integral in equation (53) is evaluated in Appendix E to give

$$\begin{aligned} & \int_{-\Delta t/2}^{\Delta t/2} e^{i2\pi \left[ (f_c - f)t + \frac{(f_1-f_0)}{2\Delta t} t^2 \right]} dt \\ &= \sqrt{\frac{\Delta t}{2(f_1-f_0)}} \exp\left[ \frac{-i\pi\Delta t(f_c-f)^2}{(f_1-f_0)} \right] \left\{ \frac{1+i}{2} \text{erf}\left[ \frac{\sqrt{\pi}}{2} (1-i) \sqrt{\frac{2\Delta t}{f_1-f_0}} \left( \frac{(f_1-f_0)}{\Delta t} t + f_c - f \right) \right] \right\}_{-\Delta t/2}^{\Delta t/2}. \end{aligned} \quad (54)$$

The scattered pressure frequency components are

$$P_s(f) = p_s(f) \int_{-\Delta f/2}^{\Delta f/2} e^{i2\pi \left[ (f_c - f)t + \frac{(f_1 - f_0)}{2\Delta t} t^2 \right]} dt \quad (55)$$

where  $p_s$  is again given by equation (12). As a function of time

$$P_s(t) = \int_{-\infty}^{\infty} P_s(f) \left\{ \int_{-\Delta f/2}^{\Delta f/2} e^{i2\pi \left[ (f_c - f)t + \frac{(f_1 - f_0)}{2\Delta t} t^2 \right]} dt \right\} e^{i2\pi f t} df. \quad (56)$$

In both equations (55) and (56) the integral over time can be replaced by the expression on the right hand side of equation (54).

In both equations (50) and (56) the scattered pressure varies in amplitude as a function of time. If the tone burst or chirp lasts for a time  $\Delta t$ , the backscatter target strength can be considered as

$$TS = 20 \log \left( \sqrt{\frac{\int_t^{t+\Delta t} |P_s(t')|_{\theta=180^\circ, r=1}^2 dt'}{\int_t^{t+\Delta t} |P_i(t')|^2 dt'}} \right) \quad (57)$$

$$= 20 \log \left( \sqrt{\frac{1}{\Delta t} \int_t^{t+\Delta t} \left| \frac{P_s(t')}{P_i(t')} \right|_{\theta=180^\circ, r=1}^2 dt'} \right). \quad (58)$$

The right hand side of equation (58) is equivalent to

$$20 \log \left( r_p r_r \sqrt{\frac{1}{\Delta t} \int_t^{t+\Delta t} \left| \frac{P_s(t')|_{r=r_r}}{P_0} \right|^2 dt'} \right) \quad (59)$$

when  $\theta = 180^\circ$  and  $r_p$  and  $r_r$  are large.

It follows from equation (58) that the target strength can be calculated for any value of  $t$  corresponding to different portions of the return signal. The most intense reflections will be the specular reflection from the front of the sphere, and the first focused return from the rear of the sphere. For  $\theta = 180^\circ$  these start when

$$t = \frac{r_p + r_r - 2b}{c_1} - \frac{\Delta t}{2} \quad (60)$$

and

$$t = \frac{r_p + r_r - 2b}{c_1} + \frac{2(b-a)}{c_2} + \frac{4a - \Delta t}{c_3} \quad (61)$$

respectively. In the results reported below, the target strength of the sphere will be considered as the maximum of the two values calculated via expression (59) at these two starting times.

### 2.3 Binary Fluids

In practical applications of the above theory it is common to use a mixture of two liquids for the interior fluid. For a binary liquid solution the longitudinal sound speed of the interior fluid becomes

$$c_3 = \left( \frac{\rho_3}{M_3} v_{mM,3} \right)^3 \quad (62)$$

where

$$\rho_3 = \frac{V_{3,a}\rho_{3,a} + V_{3,b}\rho_{3,b}}{V_{3,a} + V_{3,b}} \quad (63)$$

$$v_{mM,3} = v_{m,3a}N_{3,a} + v_{m,3b}N_{3,b} \quad (64)$$

$$M_3 = N_{3,a}M_{3,a} + N_{3,b}M_{3,b}. \quad (65)$$

$V_{3,a}$  and  $V_{3,b}$  are the volumes of the two liquids,  $\rho_{3,a}$  and  $\rho_{3,b}$  are their densities,  $v_{m,3a}$  and  $v_{m,3b}$  are their molecular velocities,  $N_{3,a}$  and  $N_{3,b}$  are the mole fractions, and  $M_{3,a}$  and  $M_{3,b}$  are the molecular masses. In general, the densities and velocities are a function of temperature, so the speed of sound of the interior fluid will likewise be temperature dependent.

## 3. Physical Data

Consider a spherical shell filled with a fluid or mixture of two fluids and placed in the sea. If a small sound projector directs a continuous sinusoidal, tone burst or chirped signal at it, the reflected signal picked up by a hydrophone in the same or another location will depend on a large number of factors. Parameters from the incident sound include the distance from the source to the centre of the sphere, the frequency for a continuous signal, the frequency and pulse length for a tone burst, and the start and stop frequencies and pulse length for a chirped signal. The distance from the centre of the sphere and angular position of the receiver are other factors, as are a number associated with the reflecting sphere. These include the diameter, thickness, and

material out of which the shell is made. The latter factor determines the density of the shell, as well as Poisson's ratio for the material, and the velocity of longitudinal and shear waves in it. The temperature, salinity and depth of the propagation path set the density and sound velocity of the fluid surrounding the sphere. The temperature and the filling fluid or mixture of fluids chosen affect the interior fluid's density and sound velocity.

Clearly, when long projector-to-sphere ranges are used, sound absorption in the water may be significant. As this will not affect a comparison of different sphere/filling fluid/signal type parameters, it has not been included in the calculations reported. Nor has absorption within the sphere or its filling fluid, as the ranges considered are so small.

Table 1 lists the parameters for the shell materials studied. For the fluids the density and sound velocity depend on a number of factors, as noted above, so equations are needed to express these dependences. Millero and Poisson (1981) give the density of sea water (in  $\text{kg m}^{-3}$ ) as

$$\rho_1 = \left( \frac{\rho^0}{1 - \frac{P}{K}} \right) \quad (66)$$

where

$$\begin{aligned} \rho^0 = & 999.842594 + 6.793952 \times 10^{-2} t - 9.095290 \times 10^{-3} t^2 + 1.001685 \times 10^{-4} t^3 \\ & - 1.120083 \times 10^{-6} t^4 + 6.536336 \times 10^{-9} t^5 + (8.24493 \times 10^{-1} - 4.0899 \times 10^{-3} t \\ & + 7.6438 \times 10^{-5} t^2 - 8.2467 \times 10^{-7} t^3 + 5.3875 \times 10^{-9} t^4) S + (-5.72466 \times 10^{-3} \\ & + 1.0227 \times 10^{-4} t - 1.6546 \times 10^{-6} t^2) S^{3/2} + 4.8314 \times 10^{-4} S^2 \end{aligned} \quad (67)$$

$$\begin{aligned} K = & 19652.21 + 148.4206 t - 2.327105 t^2 + 1.360477 \times 10^{-2} t^3 - 5.155288 \times 10^{-5} t^4 \\ & + S (54.6746 - 0.603459 t + 1.09987 \times 10^{-2} t^2 - 6.1670 \times 10^{-5} t^3) + S^{3/2} (7.944 \times 10^{-2} \\ & + 1.6483 \times 10^{-2} t - 5.3009 \times 10^{-4} t^2) + P [3.239908 + 1.43713 \times 10^{-3} t + 1.16082 \times 10^{-4} t^2 \\ & - 5.77905 \times 10^{-7} t^3 + S (2.2838 \times 10^{-3} - 1.0981 \times 10^{-5} t - 1.6078 \times 10^{-6} t^2) \\ & + S^{3/2} (1.91075 \times 10^{-4})] + P^2 [8.50935 \times 10^{-5} - 6.12293 \times 10^{-6} t + 5.2787 \times 10^{-8} t^2 \\ & + S (-9.9348 \times 10^{-7} + 2.0816 \times 10^{-8} t + 9.1697 \times 10^{-10} t^2)] \end{aligned} \quad (68)$$

and

$$P = \int_0^d \rho_1 g dy. \quad (69)$$

$P$  is the gauge pressure in bars, with  $P=0$  at the water surface under 1 atm of air pressure. A rough rule of thumb is that the pressure increases by 1 bar for every 10 m of water depth.  $S$  is the salinity in ‰,  $t$  is the temperature in °C,  $d$  is the depth in m and  $g$  is the acceleration due to gravity. The speed of sound (in  $\text{ms}^{-1}$ ) is given as

$$c_1 = 1412 + 3.21t + 1.19S + 0.0167d \quad (70)$$

by Francois and Garrison (1982).

Table 1:

Material	Density ( $\text{kg m}^{-3}$ )	Poisson's ratio	Velocity of longitudinal waves ( $\text{ms}^{-1}$ )	Velocity of shear waves ( $\text{ms}^{-1}$ )
Aluminium	2700	0.355	6420	3040
Brass	8600	0.374	4700	2110
Nickel	8900	0.336	6040	3000
Pyrex glass	2320	0.17	5640	3280
Steel	7910	0.29	5790	3100

The above data were obtained from Gray (1972).

To achieve a high target strength in the backscatter direction, a filling fluid with a refractive index between 1.5 and 2.0 is needed to obtain the necessary thin lens focusing. This is most easily accomplished by mixing two liquids of different sound speeds, one above and the other below the required speed. Other considerations are cost and safety of the liquids. Some of the potential liquids, such as  $\text{CCl}_4$ , are hazardous. Initially Freon-113™ and ethanol, mixed in varying ratios, were studied as the filling liquid, as they are cheap, relatively safe and readily available. However due to expected difficulties in obtaining Freon-113™, Fluorinert FC-72™ and n-hexane have also been studied. From Gray (1972) the density and speed of sound in ethanol are

$$\rho_{3,a} = 785.06 - 0.8591(t-25) - 5.6 \times 10^{-4}(t-25)^2 - 5 \times 10^{-6}(t-25)^3 \quad \text{for } 10 < t < 40 \quad (71)$$

and

$$c_{3,a} = 1232.13 - 3.5739t + 2.39 \times 10^{-3}t^2 + 2.65 \times 10^{-5}t^3 - 2.4 \times 10^{-7}t^4 \quad \text{for } 0 < t < 58. \quad (72)$$

Fitting curves to the data of Leader *et al.* (1969), the density and speed of sound in Freon-113™ are

$$\rho_{3,b} = 1614.5 - 2.04t \quad \text{for } 0 \leq t \leq 40 \quad (73)$$

and

$$c_{3,b} = \begin{cases} 786.1 - 3.345t & \text{for } 0 \leq t \leq 20 \\ 778.7 - 2.975t & \text{for } 20 \leq t \leq 40 \end{cases} \quad (74)$$

Fitting a curve to the data of Timmermans (1950), the density of n-hexane is

$$\rho_{3,a} = 676.891 - 0.846t - 1.1 \times 10^{-3}t^2. \quad (75)$$

Kaye and Laby (1973) quote the speed of sound in it at 30°C as 1060 ms<sup>-1</sup>, so using the relation

$$c = \sqrt{\frac{B}{\rho}} \quad (76)$$

where B is the bulk modulus, the speed of sound in n-hexane can be given as

$$c_{3,a} = \sqrt{\frac{650.5 \times 1060^2}{\rho_{3,a}}}. \quad (77)$$

3M's *Fluorinert<sup>TM</sup> Liquids, Product Manual* gives the density of Fluorinert FC-72<sup>TM</sup> as

$$\rho_{3,b} = 1740 - 2.61t. \quad (78)$$

From the data for the speed of sound,

$$c_{3,b} = 582 - 2.8t. \quad (79)$$

In the results reported below, comparison will be made with an air-filled sphere. At sea level, Kaye and Laby (1973) give the density of air for 50% relative humidity as

$$\rho_3 = \frac{1.29307 \times 101.3 - 0.2443 p_{sv}}{101.325} \times 1.000028 \times (1 + 0.00367t) \quad (80)$$

where the saturated vapour pressure  $p_{sv}$  can be found by fitting a curve to their data to yield

$$p_{sv} = 0.6116 + 4.365 \times 10^{-2}t + 1.567 \times 10^{-3}t^2 + 1.74 \times 10^{-5}t^3 + 5.5 \times 10^{-7}t^4. \quad (81)$$

The speed of sound in air for sound waves of frequency  $f$  is (Kneser, 1931)

$$c_3 = \sqrt{\frac{\left[ \left( \frac{f}{f_r} \right)^2 c_\infty^2 + c_0^2 \right]}{1 + \left( \frac{f}{f_r} \right)^2}} \quad (82)$$

where the zero-frequency speed can be found by substituting into the equation of Miller (1937) to yield

$$c_0 = 331.46 \times \sqrt{\left( 1 + \frac{t}{273} \right) \times \left[ 1 - \frac{0.5p_{sv}}{101.3} \times \left( \frac{1.324}{1.403} - \frac{18.01534}{28.9644} \right) \right]}. \quad (83)$$

The infinite-frequency speed  $c_\infty$  exceeds this by  $0.12 \text{ ms}^{-1}$  at  $20^\circ\text{C}$  (Harris, 1971). The relaxation frequency at 50% relative humidity is (Piercy, 1969)

$$f_r = 3.05 \times 10^4 \left( \frac{50p_{sv}}{0.5p_{sv} + 101.325} \right)^{1.3}. \quad (84)$$

## 4. Computational Considerations

The summation in equation (12) is theoretically over an infinite number of terms, although in practice the summation was halted when the relative difference of the scattered pressure after summation to the  $l$ th and  $l-1$ th terms was less than 0.01% and after summation to the  $l-1$ th and  $l-2$ th terms was also less than 0.01%. To ensure convergence care had to be taken in calculating the spherical Bessel functions and their derivatives. Details of the techniques used are given in Appendix D.

As a check on the formulae, computational techniques and the computer programs used to calculate the results presented in the next section, the magnitude of the form function, defined by

$$|f_\infty| = \frac{2}{k_{L,1} b} \left| \sum_{l=0}^{\infty} (-1)^l (2l+1) C_l \right| \quad (85)$$

was calculated for an iron shell of 20 cm diameter, 20 mm wall thickness, longitudinal and shear wave sound speeds of  $5950$  and  $3240 \text{ ms}^{-1}$ , respectively, and Poisson ratio of 0.292. This shell was immersed and filled with water of density  $1000 \text{ kg m}^{-3}$  and sound speed  $1410 \text{ ms}^{-1}$ . The results are displayed in Fig. 2 along with those of

Hickling (1964) for a similar set of parameters. The agreement is generally good, although there are some variations attributed to two sources. The magnitude and position of some of the peaks and troughs do not align perfectly, due to a small inconsistency in Hickling's shear and Lamé elastic constants and longitudinal and shear sound speeds for iron. In addition, the narrow spikes are sensitive to the evaluation frequency, which was not identical for both data sets.

## 5. Results

Fig. 3 shows the calculated absolute value of the scattered pressure field in a 4 m by 4 m section centred about a stainless steel spherical shell of 20 cm diameter and 0.8 mm wall thickness. The sphere is indicated by the white circle and is filled with a mixture of 34% Fluorinert FC-72™ and 66% n-hexane by volume and deployed at shallow depths in sea water of 20°C and 35‰ salinity. The ratio of filling fluids was chosen to give a refractive index of 1.8 at 20°C. The projector is located 1000 m to the left of the origin and 1 m from it (the projector) the amplitude was unity. The scattered pressure amplitudes are relative to this value. The projector emits continuous waves of 100 kHz frequency. The field shows strong focusing in the forward scattering direction, as well as the presence of weak intensity regions and nodes. There is also some focusing in the backscatter direction.

Fig. 4 shows the scattered pressure amplitude field with the same sphere and environment parameters. The projector emits continuous waves of 200 kHz. Note the narrower focusing in the backscatter direction.

Fig. 5 displays the total (incident plus scattered) pressure amplitude field in a section through the centre of the sphere, in the vicinity of the sphere, whose inner and outer walls are shown by the black circles. The parameters are as for Fig. 3. The waves to the left show what may be spherical spreading but with a radius of curvature slightly larger than that of the sphere. To the right of the sphere the nodes and antinodes form a pattern radial from a point somewhat to the left of the centre of the sphere. The wave pattern inside the sphere is complex. A set of nodes and antinodes occurs both radially and circumferentially, with the greatest intensity along the axis from the projector.

Fig. 6 shows the total pressure amplitude field under the same conditions for continuous waves of 200 kHz. The features are similar to that for Fig. 5, but on a smaller scale commensurate with the higher frequency.

Fig. 7 overlays four sets of calculated backscattered target strength values for a projector and receiver collocated 1000 m from a sphere. The sphere is of stainless steel of 20 cm diameter and 0.8 mm wall thickness and is filled with a mixture of 68% Freon-113™ and 32% ethanol by volume and deployed at shallow depths in sea water of 20°C and 35‰ salinity. The ratio of filling fluids was chosen to give a refractive index of 1.8 at 20°C.

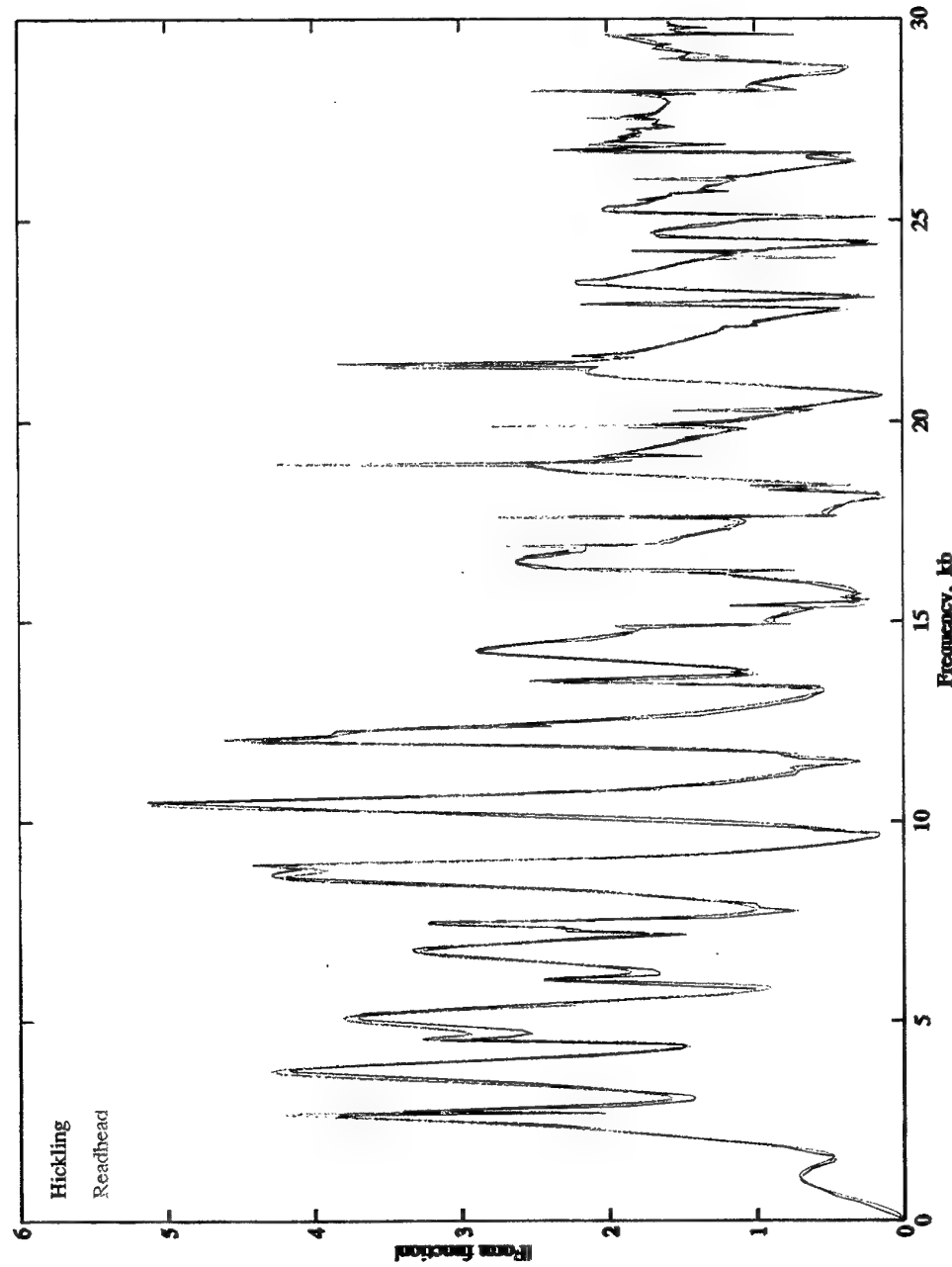


Figure 2: Magnitude of the form function for an iron shell of 20 cm diameter and 20 mm wall thickness, immersed and filled with water of density  $1000 \text{ kg m}^{-3}$  and sound speed  $1410 \text{ m s}^{-1}$ . The longitudinal and shear wave speeds of the shell are  $5950$  and  $3240 \text{ m s}^{-1}$ , respectively, and Poisson ratio is  $0.292$ . Results are compared with those of Hickling (1964). The frequency units are the product of the wavenumber and the outer radius of the sphere.

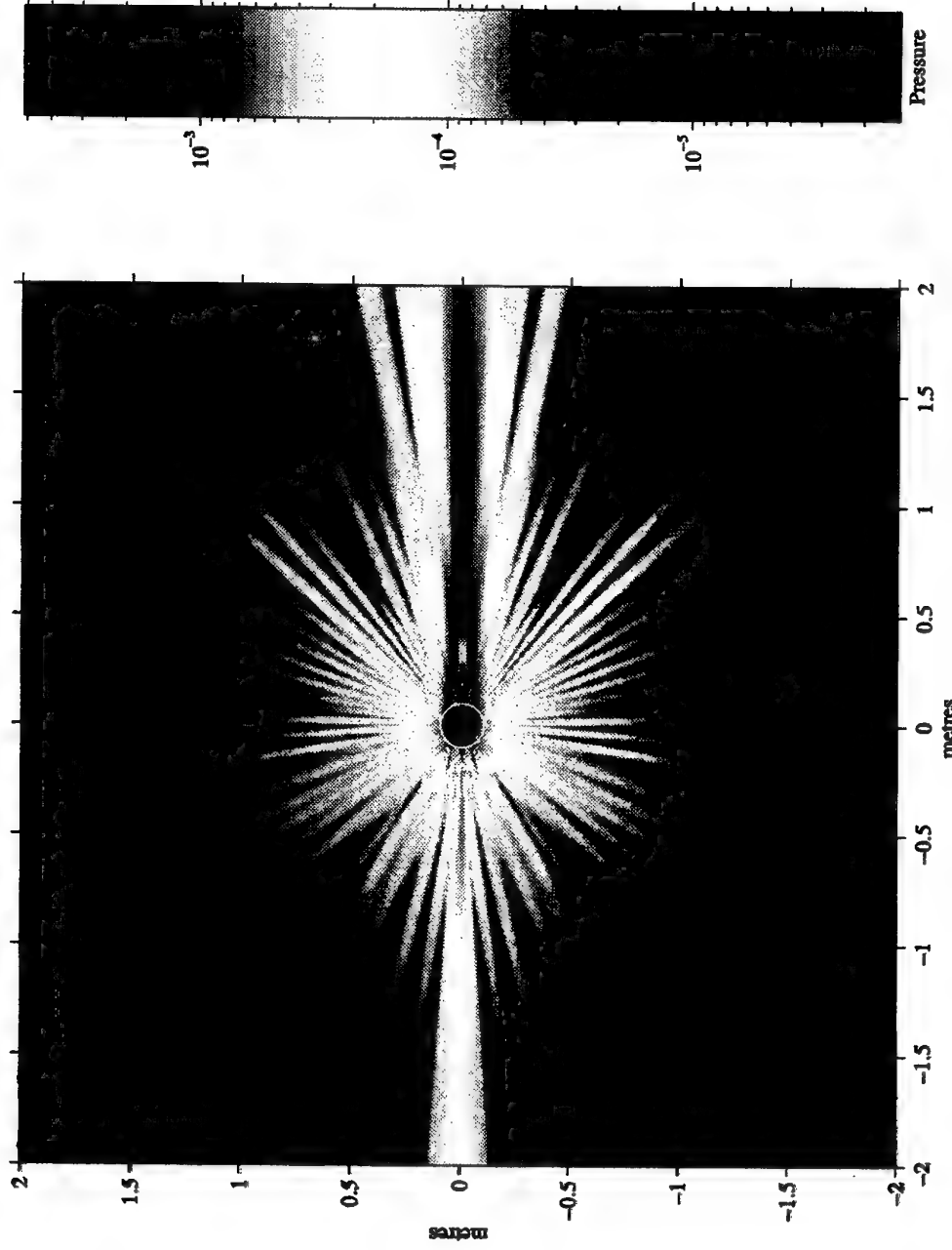


Figure 3: Scattered pressure amplitude field around a stainless steel spherical shell of 20 cm diameter and 0.8 mm wall thickness filled with 34% Fluorinert FC-77™ and 66% *n*-hexane by volume and deployed at shallow depths in sea water of 20°C and 35‰ salinity. The projector is 1000 m to the left of the origin and continuously emits 100 kHz waves, whose amplitude 1 m from it is 1. The spherical shell is indicated by the white circle.

THIS PAGE LEFT INTENTIONALLY BLANK

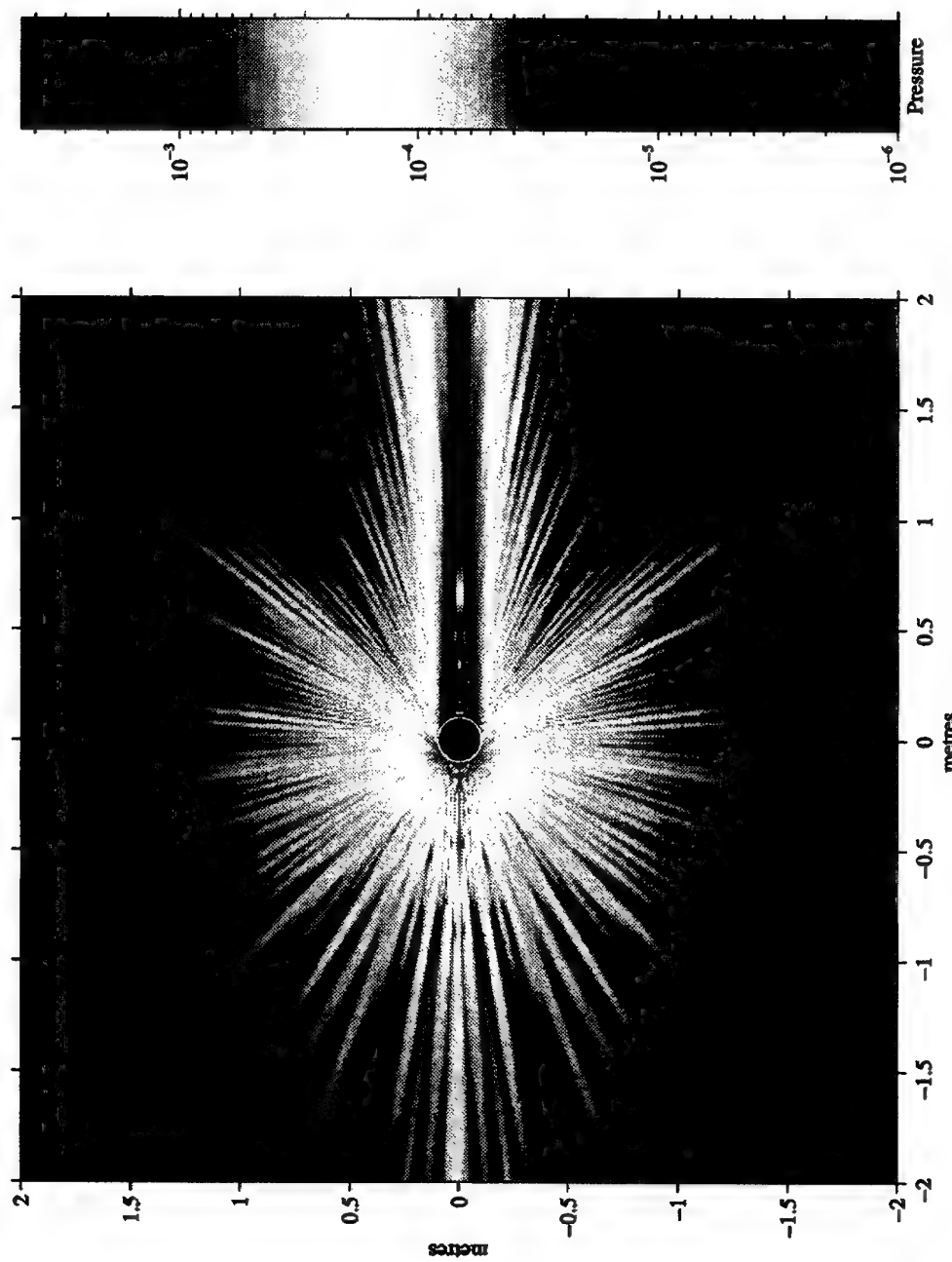


Figure 4: Scattered pressure amplitude field around a stainless steel spherical shell of 20 cm diameter and 0.8 mm wall thickness filled with 34% Fluorinert FC-77™ and 66% n-hexane by volume and deployed at shallow depths in sea water of 20°C and 35‰ salinity. The projector is 1000 m to the left of the origin and continuously emits 200 kHz waves, whose amplitude 1 m from it is 1. The spherical shell is indicated by the white circle.

THIS PAGE LEFT INTENTIONALLY BLANK

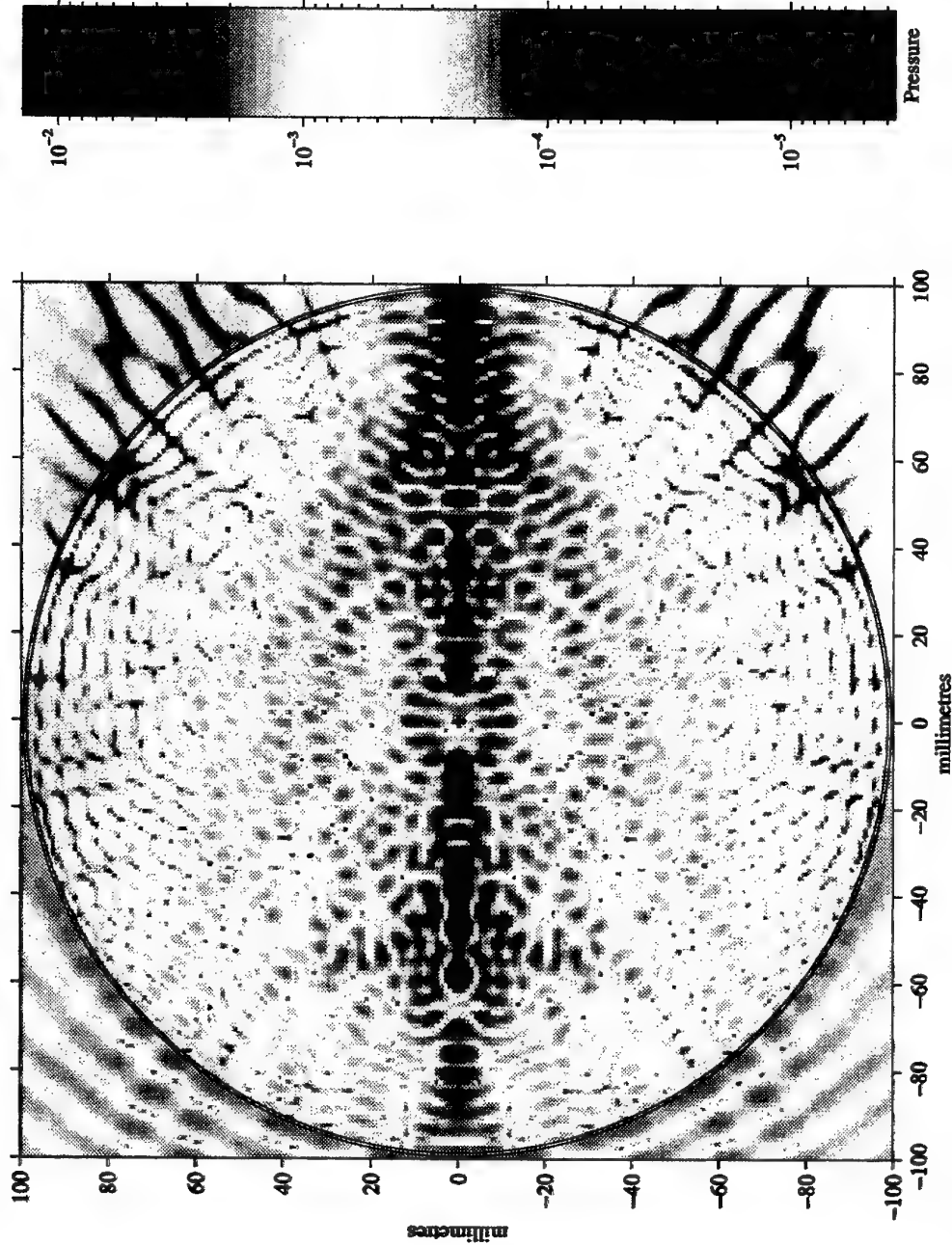


Figure 5: Total pressure amplitude field near and within a stainless steel sphere of 20 cm diameter and 0.8 mm wall thickness filled with 34% Fluorinert FC-72™ and 66% n-hexane by volume and deployed at shallow depths in sea water of 20°C and 35‰ salinity. The projector is 1000 m to the left of the origin and continuously emits 100 kHz waves, whose amplitude 1 m from it is 1. The interior and exterior walls of the spherical shell are indicated by the black circles.

THIS PAGE LEFT INTENTIONALLY BLANK

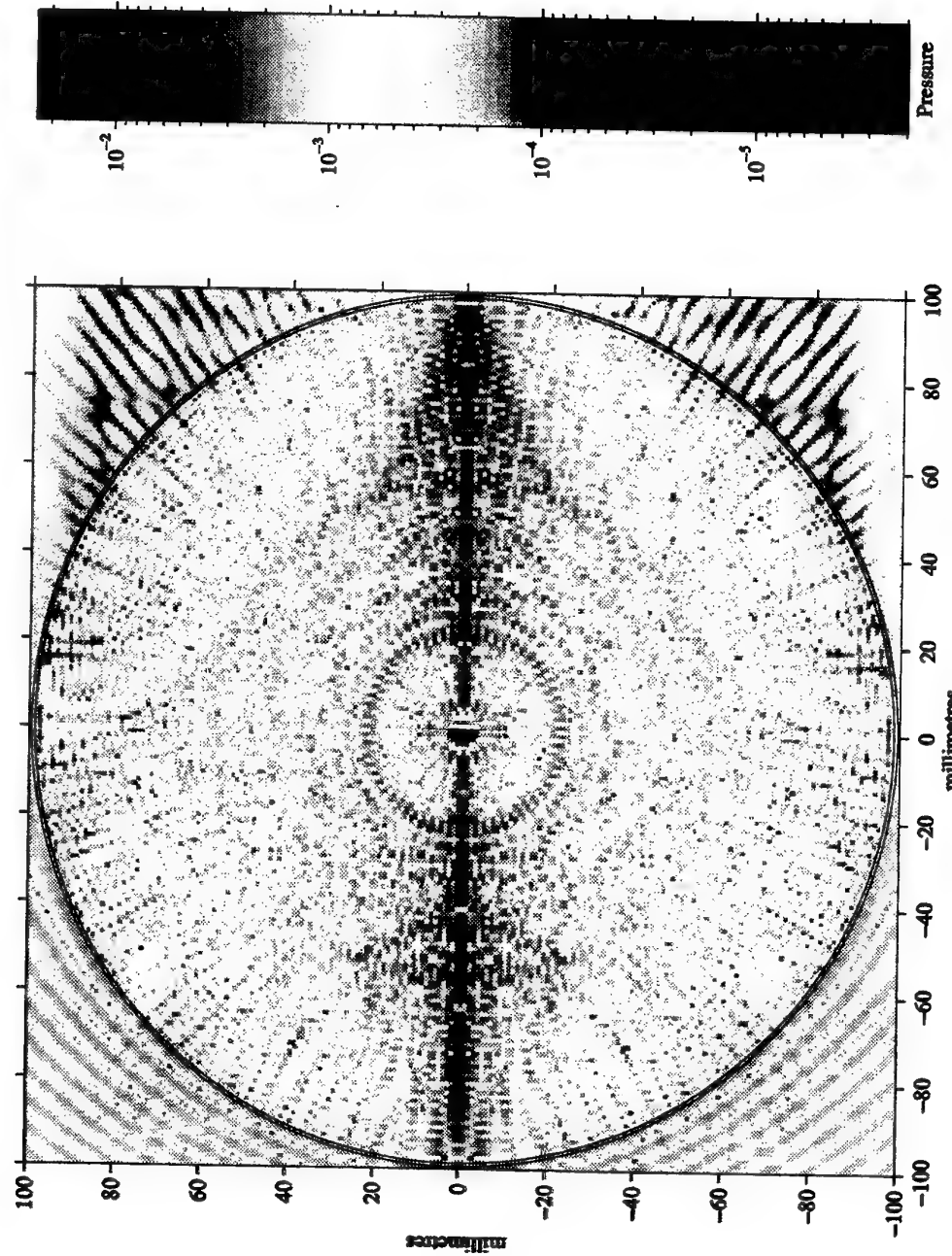


Figure 6: Total pressure amplitude field near and within a stainless steel sphere of 20 cm diameter and 0.8 mm wall thickness filled with 34% Fluorinert FC-72™ and 66% *n*-hexane by volume and deployed at shallow depths in sea water of 20°C and 35‰ salinity. The projector is 1000 m to the left of the origin and continuously emits 200 kHz waves, whose amplitude 1 m from it is 1. The interior and exterior walls of the spherical shell are indicated by the black circles.

THIS PAGE LEFT INTENTIONALLY BLANK

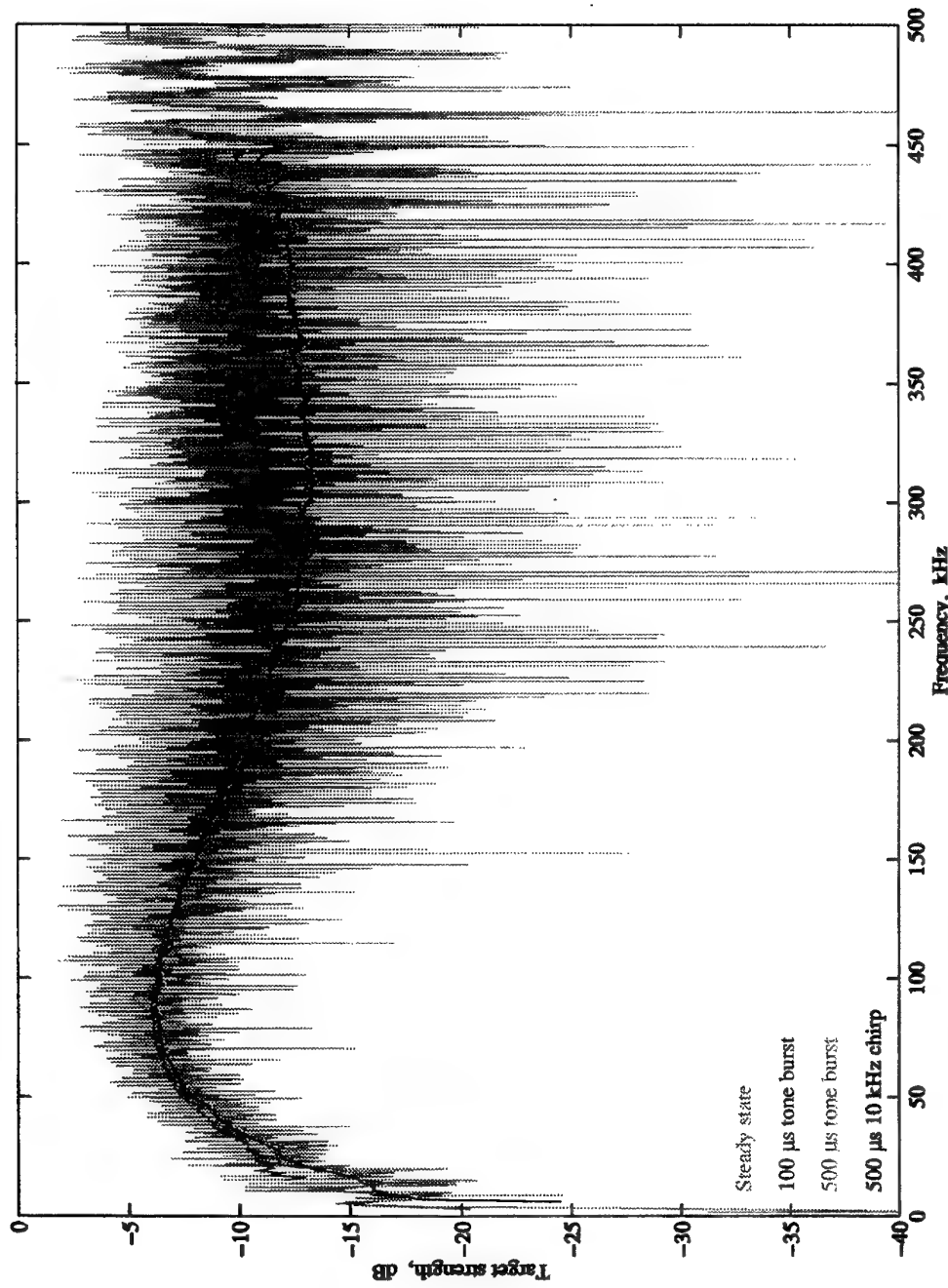


Figure 7: Target strength of a stainless steel spherical shell of 20 cm diameter and 0.8 mm wall thickness filled with 68% Freon-113™ and 32% ethanol by volume and deployed at shallow depths in sea water of 20°C and 35‰ salinity. The target strength is shown under steady state conditions, for 100 and 500  $\mu$ s tone bursts, and 10 kHz bandwidth chirps of 500  $\mu$ s duration.

THIS PAGE LEFT INTENTIONALLY BLANK

The wildly varying line is the target strength as a function of frequency for steady state conditions. The target strength was calculated in 100 Hz steps from 100 Hz to 500 kHz. For very low frequencies the sphere is small compared to the wavelength of sound in water, and very little sound is reflected. With increasing frequency the target strength increases, but fluctuates wildly with small changes in the frequency. Beyond 450 kHz it takes on an oscillatory nature.

The target strength as a function of frequency in 1 kHz steps to 450 kHz is shown for both 100 and 500  $\mu$ s tone bursts. The result for 500  $\mu$ s chirps of 10 kHz bandwidth centred on frequencies taken in 1 kHz steps to 450 kHz is also shown. Although there are small variations between the last three curves, especially below 50 kHz and above 400 kHz, these are of a minor nature.

Fig. 8 shows the fine detail of the steady state data of Fig. 7 between 100 and 120 kHz, calculated in 25 Hz steps. It is compared with data in 100 Hz steps. The overall result is the same, although several narrow spikes are evident in the former set of data. The curves indicate that most of the major target strength variations are somewhat oscillatory, with a period of approximately 1.6 kHz. Overlaid on this is a fine structure with a width of less than 25 Hz.

The target strength as a function of frequency in 1 kHz steps from 100 to 120 kHz is also shown in Fig. 8 for 100  $\mu$ s tone bursts. One curve shows the results based on steady state data calculated in 25 Hz steps; the other shows the result when the steady state data has been calculated in 100 Hz steps. The results are almost identical, indicating that the fine structure has little effect for 100  $\mu$ s tone bursts.

The complexity of the target strength as a function of frequency for both continuous and pulsed waves is due to the existence of resonances of several types, which occur in the fluid and the shell. At low frequencies "Franz" or "creeping" waves circumnavigate the shell in the external fluid. The eigenfrequencies depend upon the shape and size of the shell and correspond to constructive interference between the specularly reflected waves and those circumnavigating the sphere. "Rayleigh" and "whispering gallery" waves, which depend on the composition of an elastic target, occur at frequencies for which multiple half-integral wavelengths correspond to the circumference, thereby producing standing waves on the surface which radiate back into the fluid. These are applicable to solid elastic targets. "Lamb" waves are the analogue for the elastic shell, with extensional and flexural resonances occurring. They depend on the composition of the shell. Other resonances occur when the multiple half-integral wavelength associated with the compressional waves in the shell equals the shell thickness.

Figs 9 and 10 display the target strength as a function of frequency to 450 kHz for refractive indices of 1.5, 1.6, 1.7, 1.8 and 1.9. In each diagram the projector and sphere are deployed at shallow depths in sea water of 20°C and 35% salinity. The projector and receiver are located 1000 m away and the former emits 100  $\mu$ s tone bursts. The spherical shell is made of stainless steel and is 20 cm in diameter and of 0.8 mm wall thickness. In Fig. 9 the shell was filled with a mixture of Freon-113™ and ethanol; in Fig. 10 the filling liquids were Fluorinert FC-72™ and n-hexane. The ratios of the two

sets of liquids were chosen to give the same velocities of sound, but the densities were not identical. In general, the target strengths with the Fluorinert FC-72™ and n-hexane combination are less than for the Freon-113™ and ethanol combination, but the overall shape of each pair of curves is similar.

Figs 11 and 12 show the effect of shell material composition on the target strength for 100  $\mu$ s tone bursts of frequencies to 450 kHz. Again the projector and receiver were located 1000 m from a 20 cm diameter shell of 0.8 mm wall thickness in shallow depths of sea water of 20°C and 35% salinity. In Fig. 11 the shell was filled with 68% Freon-113™ and 32% ethanol by volume; in Fig. 12 the liquids were 34% Fluorinert FC-72™ and 66% n-hexane by volume. In each case the refractive index was 1.8. The structure of the curves is similar for each pair of liquids, but again the target strengths with the Fluorinert FC-72™ and n-hexane combination are less than for the Freon-113™ and ethanol combination. Generally, glass and aluminium yield substantially larger target strengths than for the other materials, although stainless steel and nickel are more likely to be used as targets in practice because of their greater durability.

Concentrating on stainless steel as the shell material, Fig. 13 shows the effect of varying the shell diameter. All other parameters are as for Fig. 12. As expected, the target strength increases with diameter. The oscillatory behaviour evident in Fig. 7 is very pronounced for the 10 cm diameter sphere.

Keeping to a stainless steel shell, Figs 14 and 15 display the effect of varying the wall thickness. All other parameters are as for Figs 11 and 12, respectively. Again, the Fluorinert FC-72™ - n-hexane combination results in lower target strengths than the Freon-113™ - ethanol combination. For very thin walls, which are not physically practical, the target strength increases relatively smoothly with frequency, and is less than that for thicker walls at low frequencies. As the thickness increases, the target strength rises to a maximum with frequency, then declines. The frequency and height of the maximum decreases with increasing wall thickness. As the wall thickness increases the oscillatory behaviour referred to above starts to appear, and begins at progressively lower frequencies. The curve for 1.6 mm wall thickness indicates that this oscillatory response does not continue for all higher frequencies, but only occurs over a limited frequency range, before dying out and returning to a more regular response.

Figs 16 and 17 show how the refractive index varies for changes in the percentage by volume of Freon-113™ and ethanol, and Fluorinert FC-72™ and n-hexane, respectively. The curves are plotted for waters of 35% salinity and water (and filling liquid) temperatures of 0, 5, 10, 15, 20, 25, 30 and 35°C. Both sets of curves show sensitivity of the refractive index to temperature, and since Figs 9 and 10 in turn indicate sensitivity of the target strength to refractive index, it can be expected that with all other parameters constant, the target strength will change with temperature.

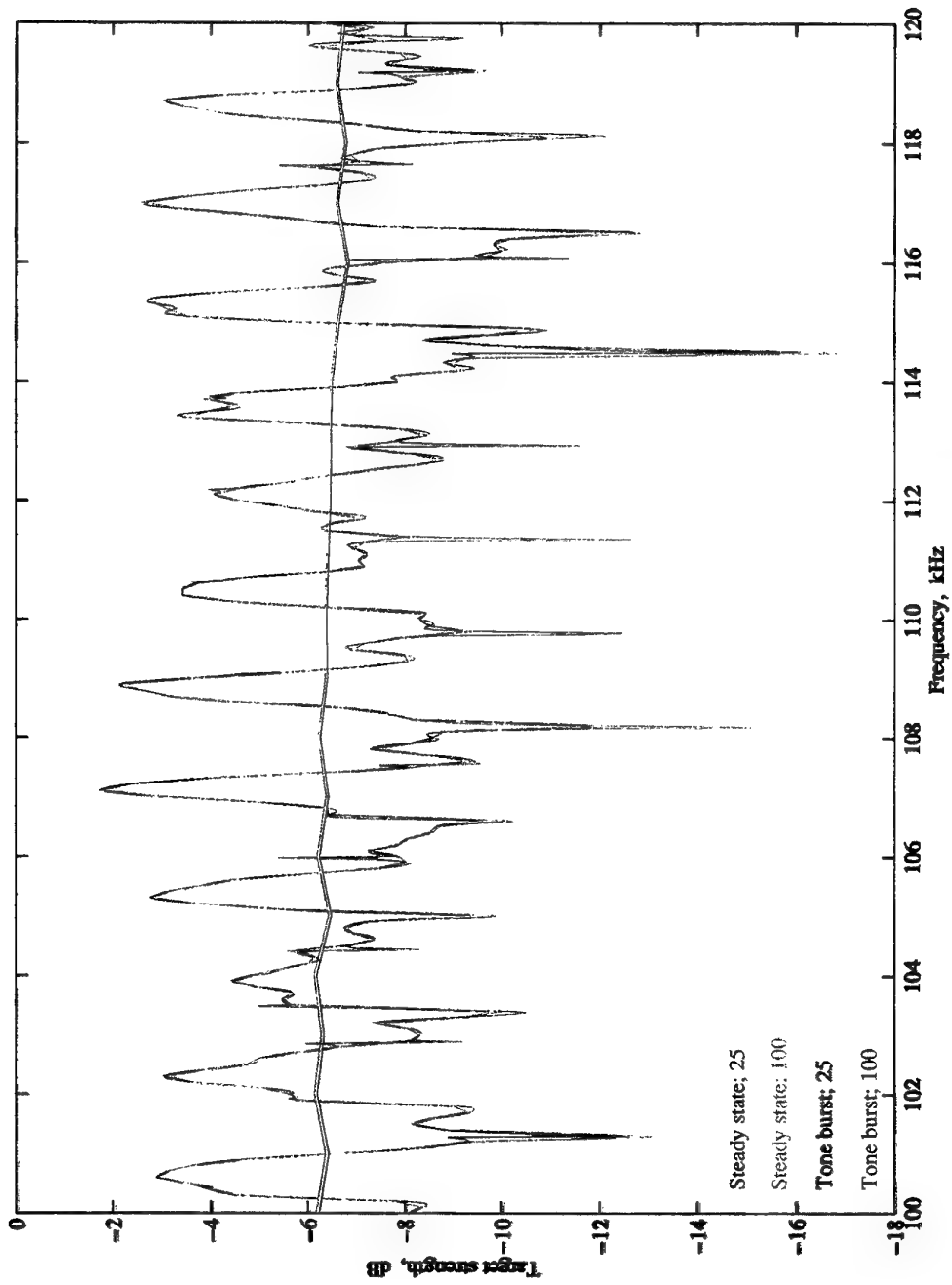


Figure 8: Target strength of a stainless steel spherical shell of 20 cm diameter and 0.8 mm wall thickness filled with 68% Freon-113™ and 32% ethanol by volume and deployed at shallow depths in sea water of 20°C and 35‰ salinity. The target strength is shown under steady state conditions in 25 and 100 Hz steps from 100 to 120 kHz, and for 100  $\mu$ s tone bursts in 1 kHz steps, based on data calculated in 25 and 100 Hz steps.

THIS PAGE LEFT INTENTIONALLY BLANK

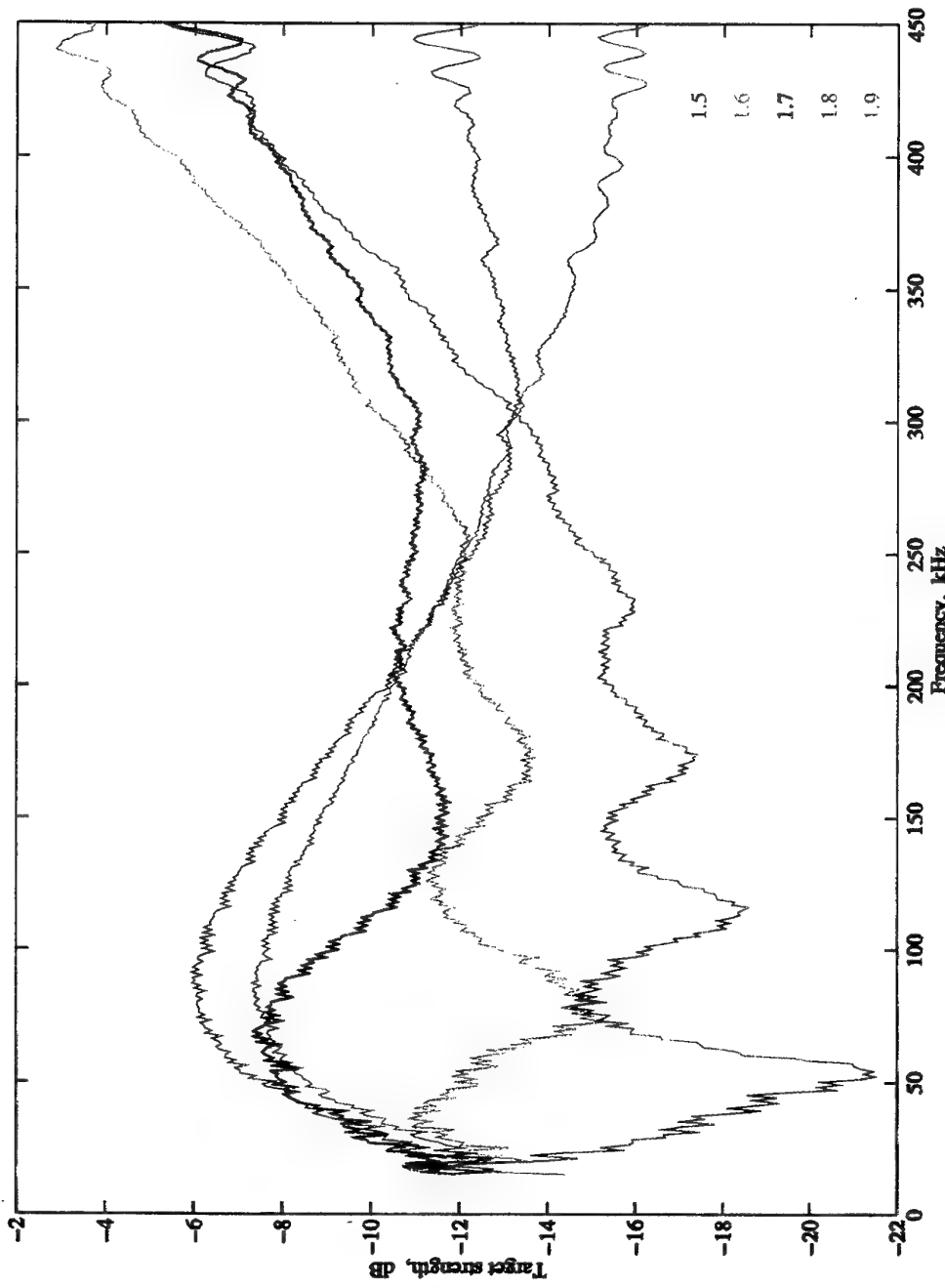


Figure 9: Variation of target strength with refractive index for a stainless steel spherical shell of 20 cm diameter and 0.8 mm wall thickness filled with a mixture of Freon-113™ and ethanol and deployed at shallow depths in sea water of 20°C and 35‰ salinity. The target strength is shown for refractive indices of 1.5, 1.6, 1.7, 1.8 and 1.9 when the incoming waves are 100  $\mu$ s tone bursts.

THIS PAGE LEFT INTENTIONALLY BLANK

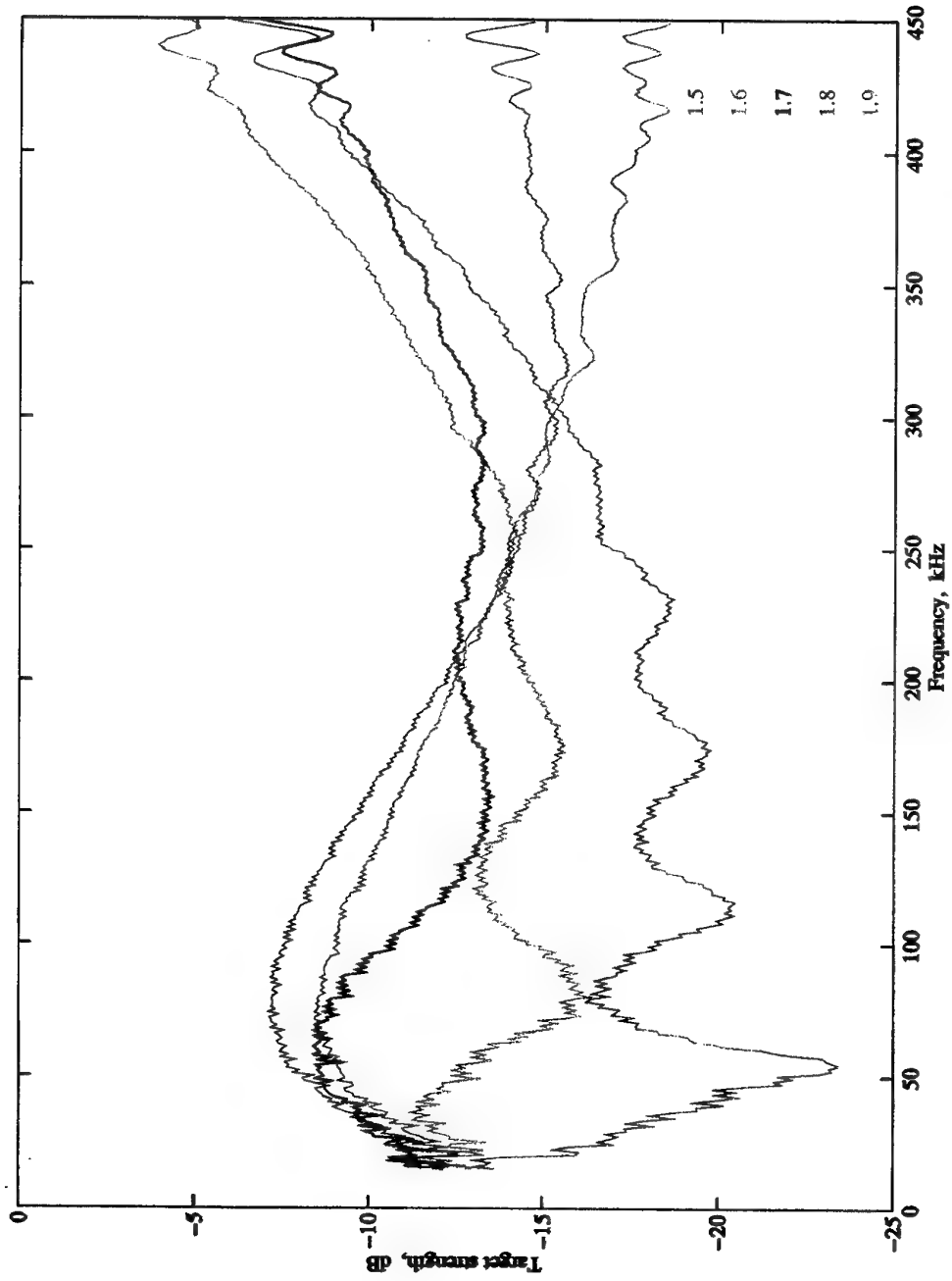


Figure 10: Variation of target strength with refractive index for a stainless steel spherical shell of 20 cm diameter and 0.8 mm wall thickness filled with a mixture of Fluorinert FC-77™ and n-hexane and deployed at shallow depths in sea water of 20°C and 35‰ salinity. The target strength is shown for refractive indices of 1.5, 1.6, 1.7, 1.8 and 1.9 when the incoming waves are 100  $\mu$ s tone bursts.

THIS PAGE LEFT INTENTIONALLY BLANK

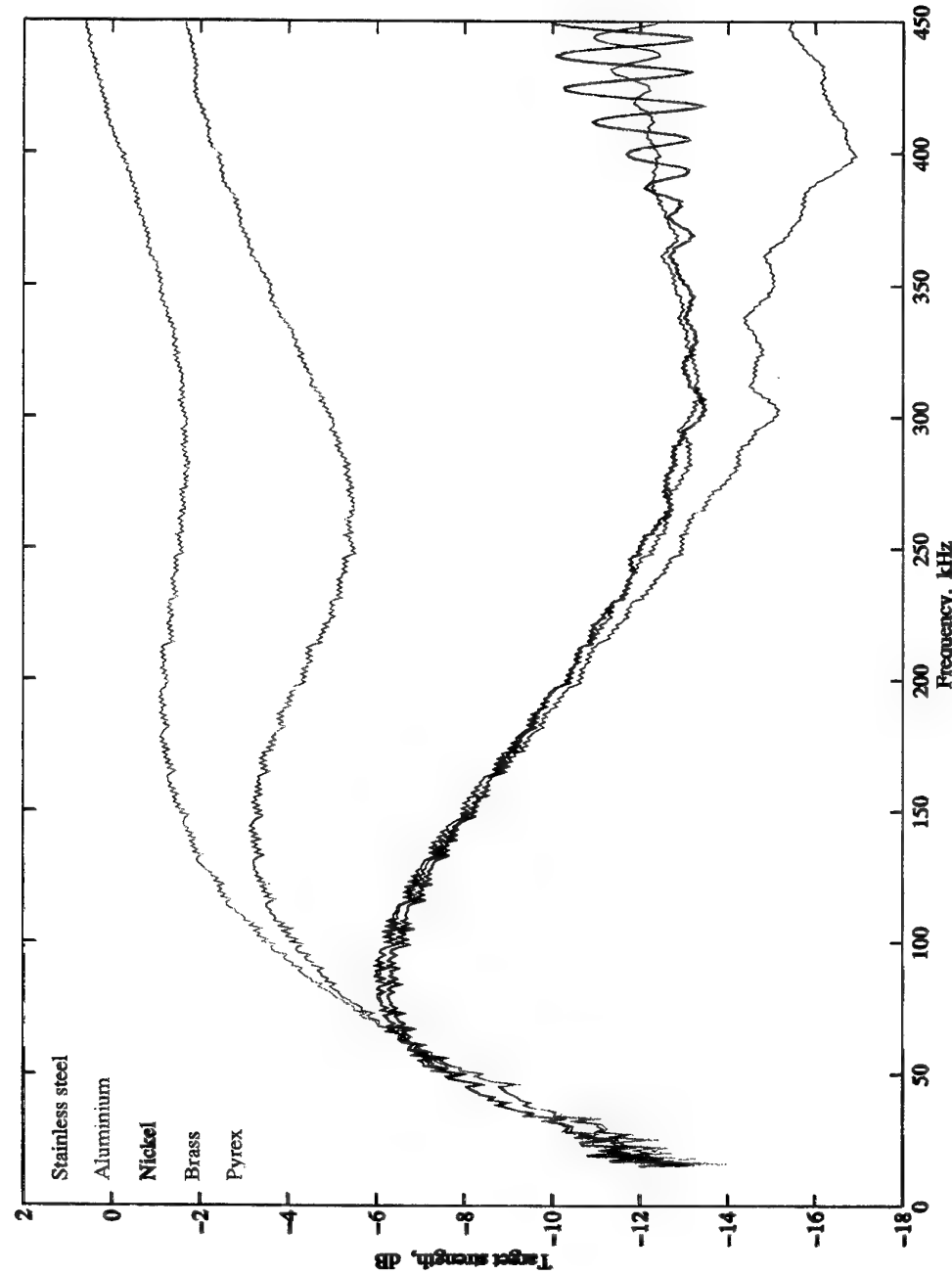


Figure 11: Variation of target strength with shell material for a spherical shell of 20 cm diameter and 0.8 mm wall thickness filled with 68% Freon-113™ and 32% ethanol by volume and deployed at shallow depths in sea water of 20°C and 35‰ salinity. The target strength is shown for the shell materials stainless steel, aluminium, nickel, brass and pyrex glass when the incoming waves are 100  $\mu$ s tone bursts.

THIS PAGE LEFT INTENTIONALLY BLANK

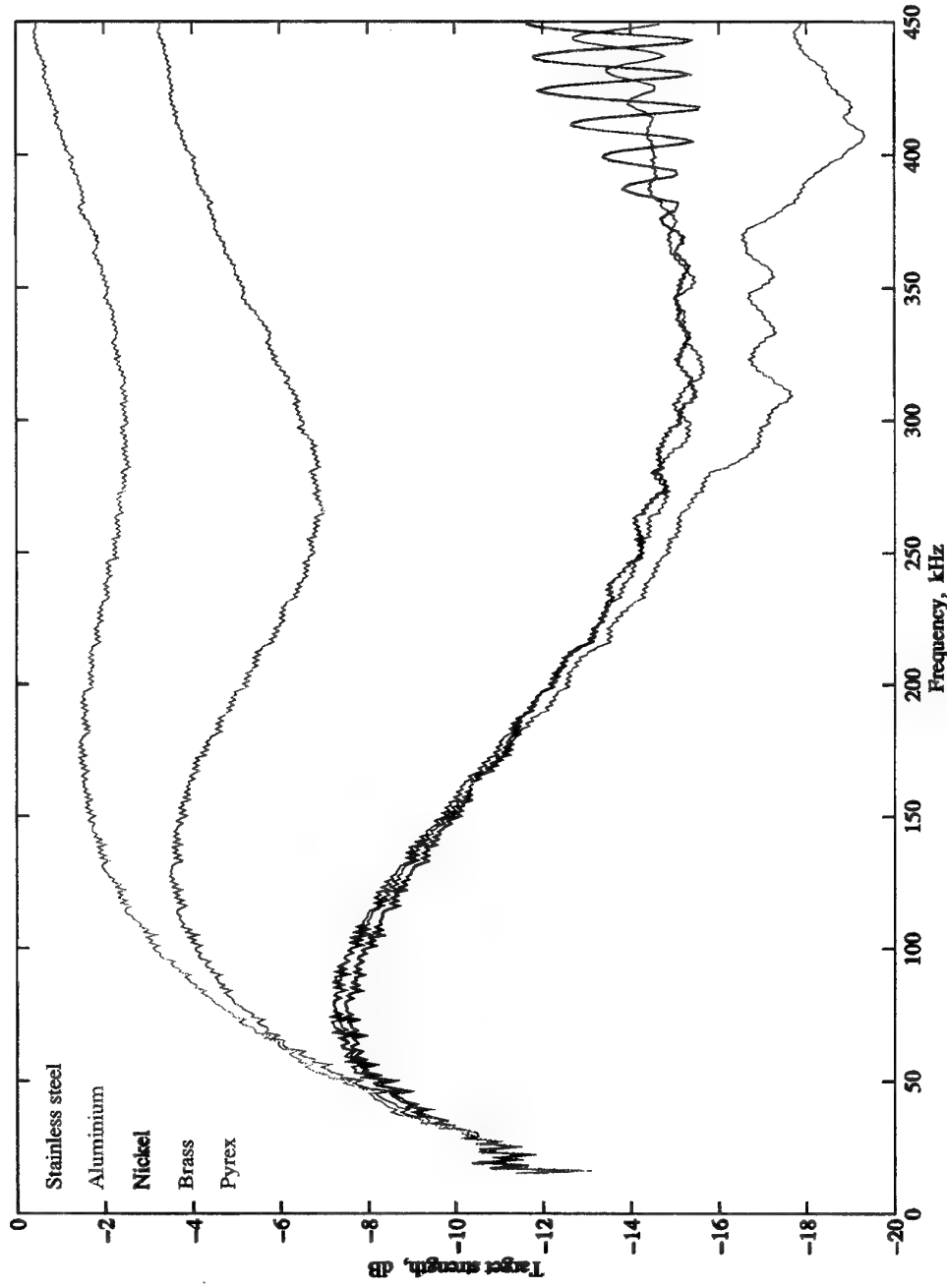


Figure 12: Variation of target strength with shell material for a spherical shell of 20 cm diameter and 0.8 mm wall thickness filled with 34% Fluorinert FC-772™ and 66% n-hexane by volume and deployed at shallow depths in sea water of 20°C and 35% salinity. The target strength is shown for the shell materials stainless steel, aluminium, nickel, brass and pyrex glass when the incoming waves are 100  $\mu$ s tone bursts.

THIS PAGE LEFT INTENTIONALLY BLANK

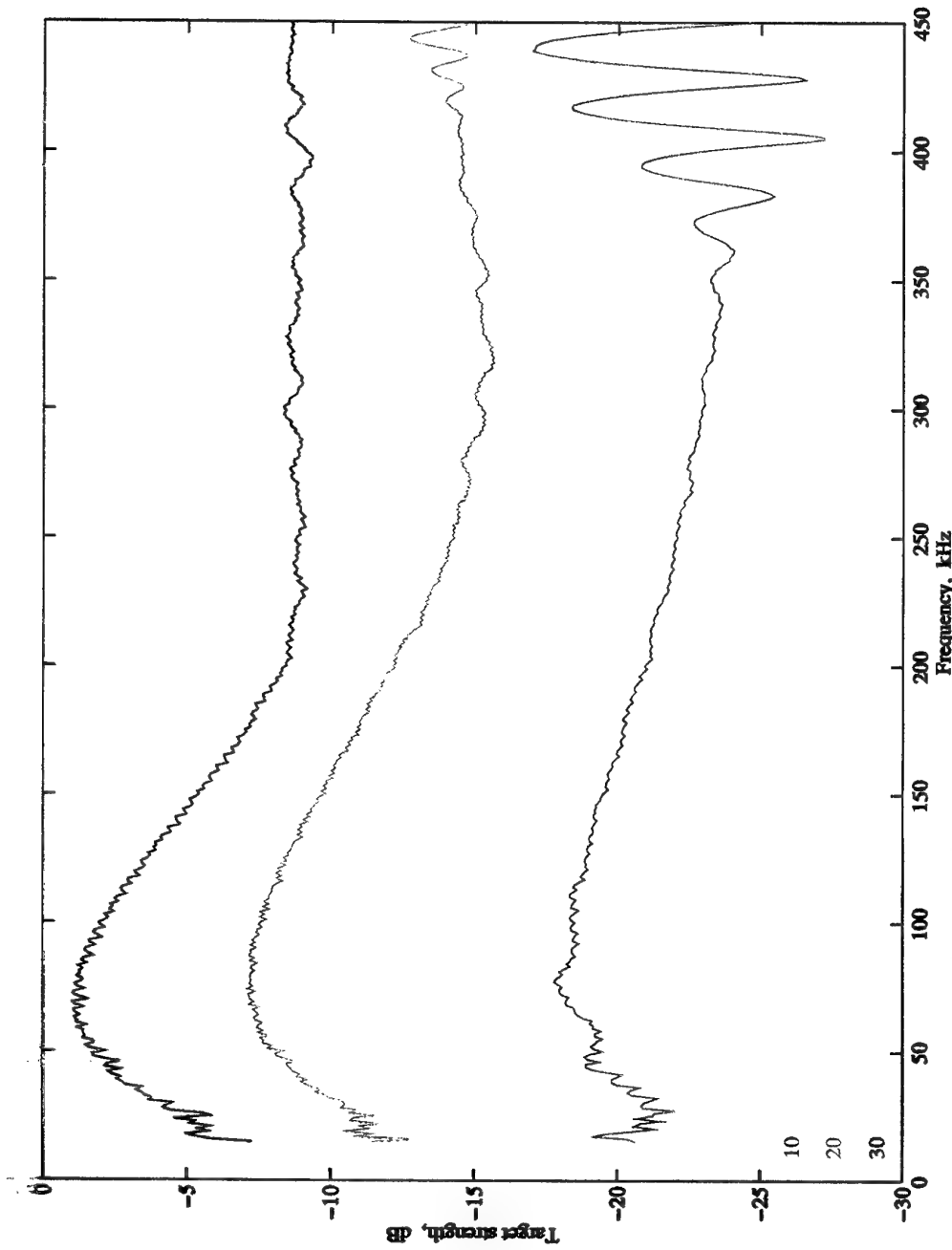


Figure 13: Variation of target strength with sphere diameter for a stainless steel spherical shell of 0.8 mm wall thickness filled with 34% Fluorinert FC-77™ and 66% n-hexane by volume and deployed at shallow depths in sea water of 20°C and 35‰ salinity. The target strength is shown for shell diameters of 10, 20 and 30 cm when the incoming waves are 100  $\mu$ s tone bursts.

THIS PAGE LEFT INTENTIONALLY BLANK

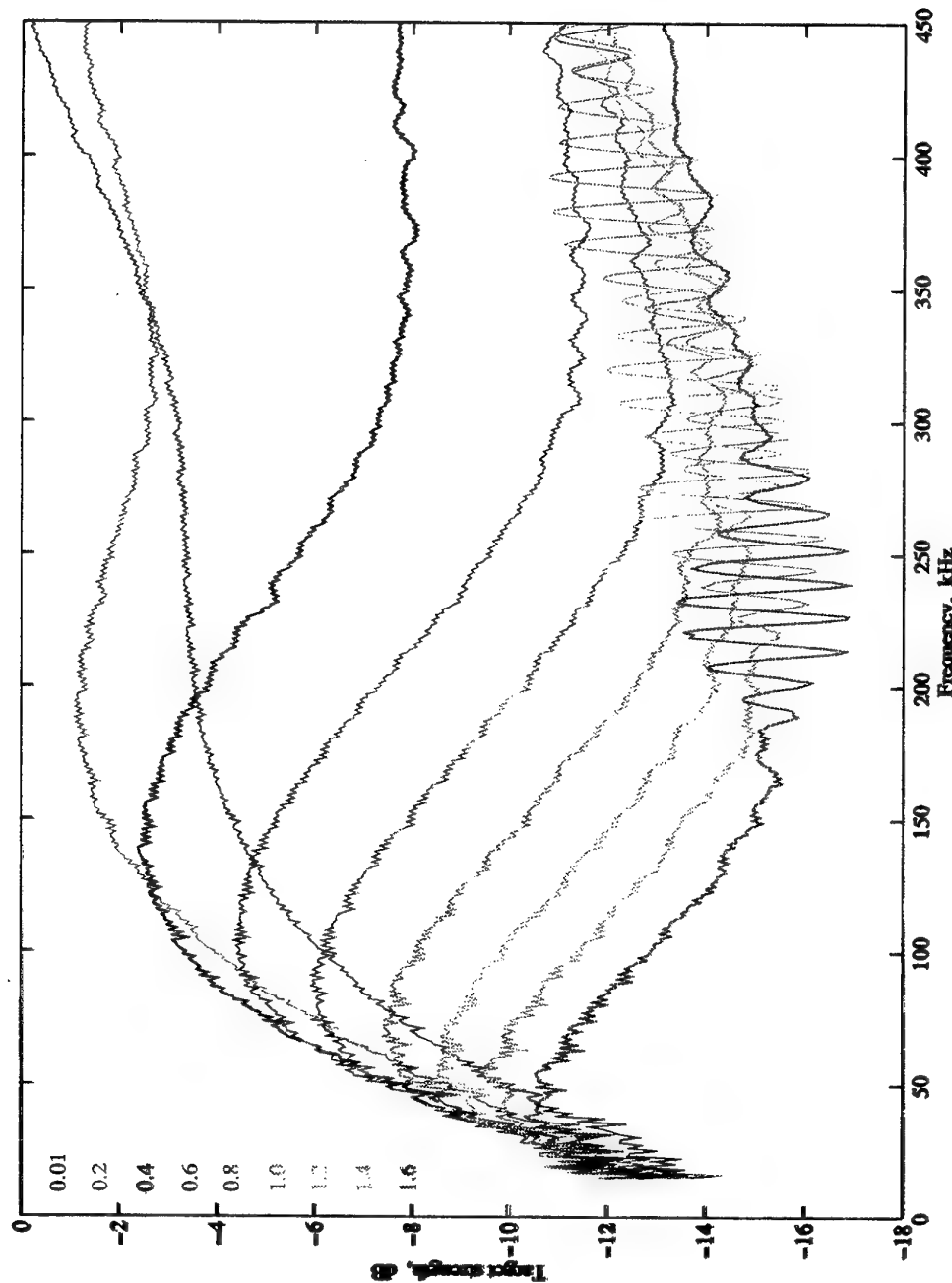


Figure 14: Variation of target strength with shell wall thickness for a stainless steel spherical shell of 20 cm diameter filled with 68% Freon-113™ and 32% ethanol by volume and deployed at shallow depths in sea water of 20°C and 35‰ salinity. The target strength is shown for wall thicknesses of 0.01, 0.2, 0.4, 0.6, 0.8, 1.0, 1.2, 1.4 and 1.6 mm when the incoming waves are 100  $\mu$ s tone bursts.

THIS PAGE LEFT INTENTIONALLY BLANK

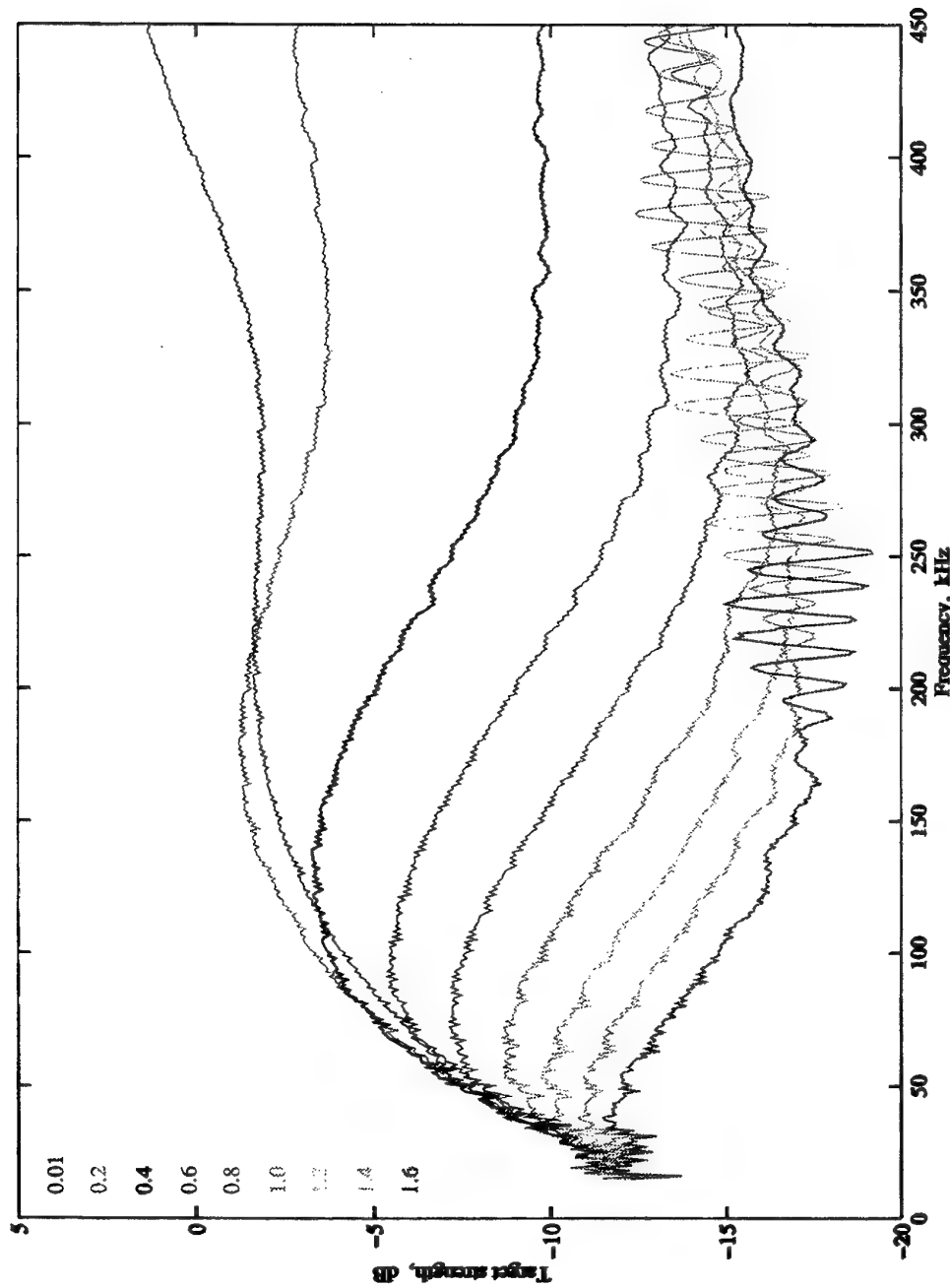


Figure 15: Variation of target strength with shell wall thickness for a stainless steel spherical shell of 20 cm diameter filled with 34% Fluorinert FC-72™ and 66% n-hexane by volume and deployed at shallow depths in sea water of 20°C and 35‰ salinity. The target strength is shown for wall thicknesses of 0.01, 0.2, 0.4, 0.6, 0.8, 1.0, 1.2, 1.4 and 1.6 mm when the incoming waves are 100  $\mu$ s tone bursts.

THIS PAGE LEFT INTENTIONALLY BLANK

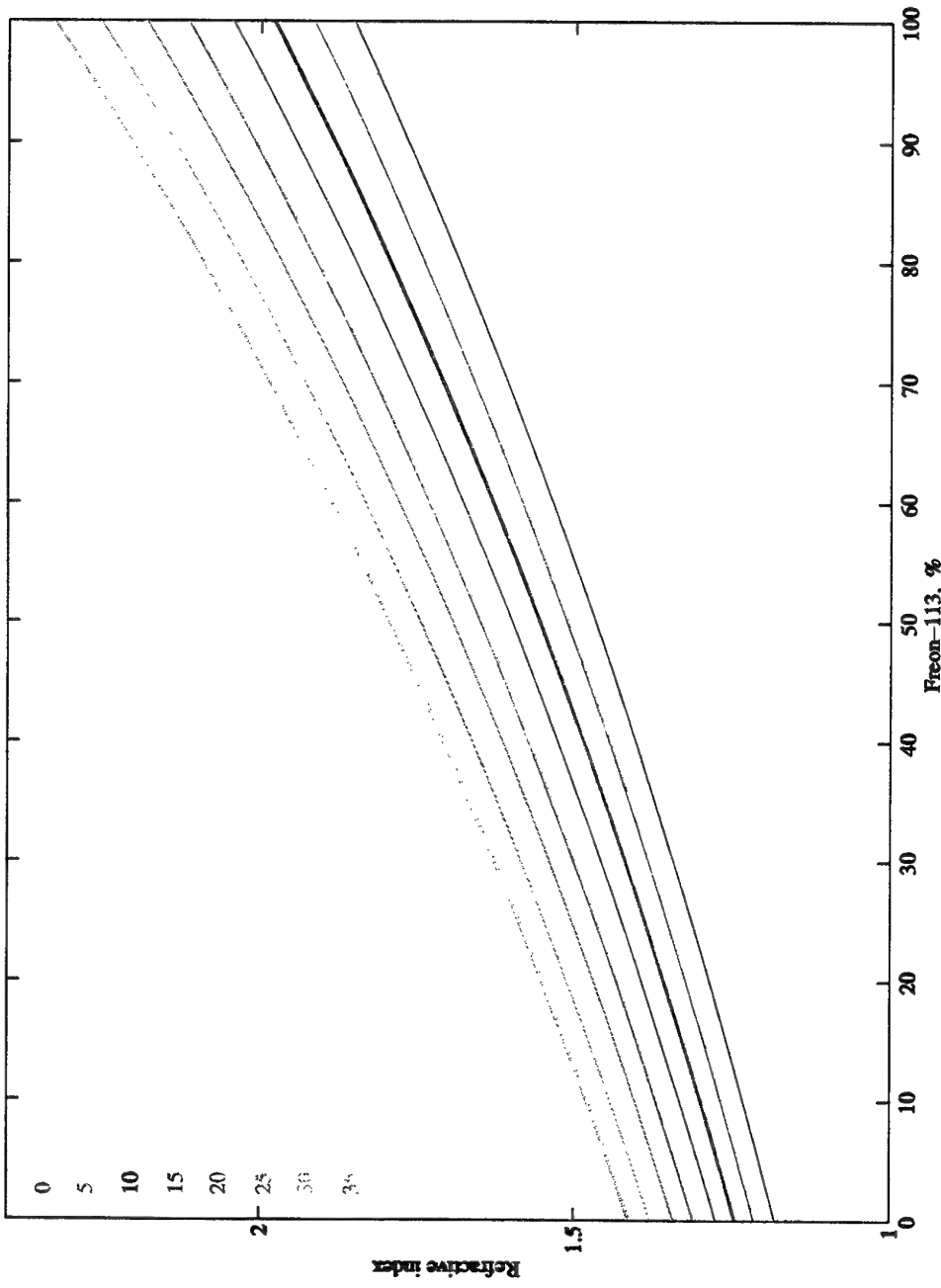


Figure 16: Refractive index as a function of the percentage of Freon-113™ in a Freon-113™ - ethanol mixture, when the mixture and exterior water of 35‰ salinity are maintained at temperatures of 0, 5, 10, 15, 20, 25, 30 and 35°C.

THIS PAGE LEFT INTENTIONALLY BLANK

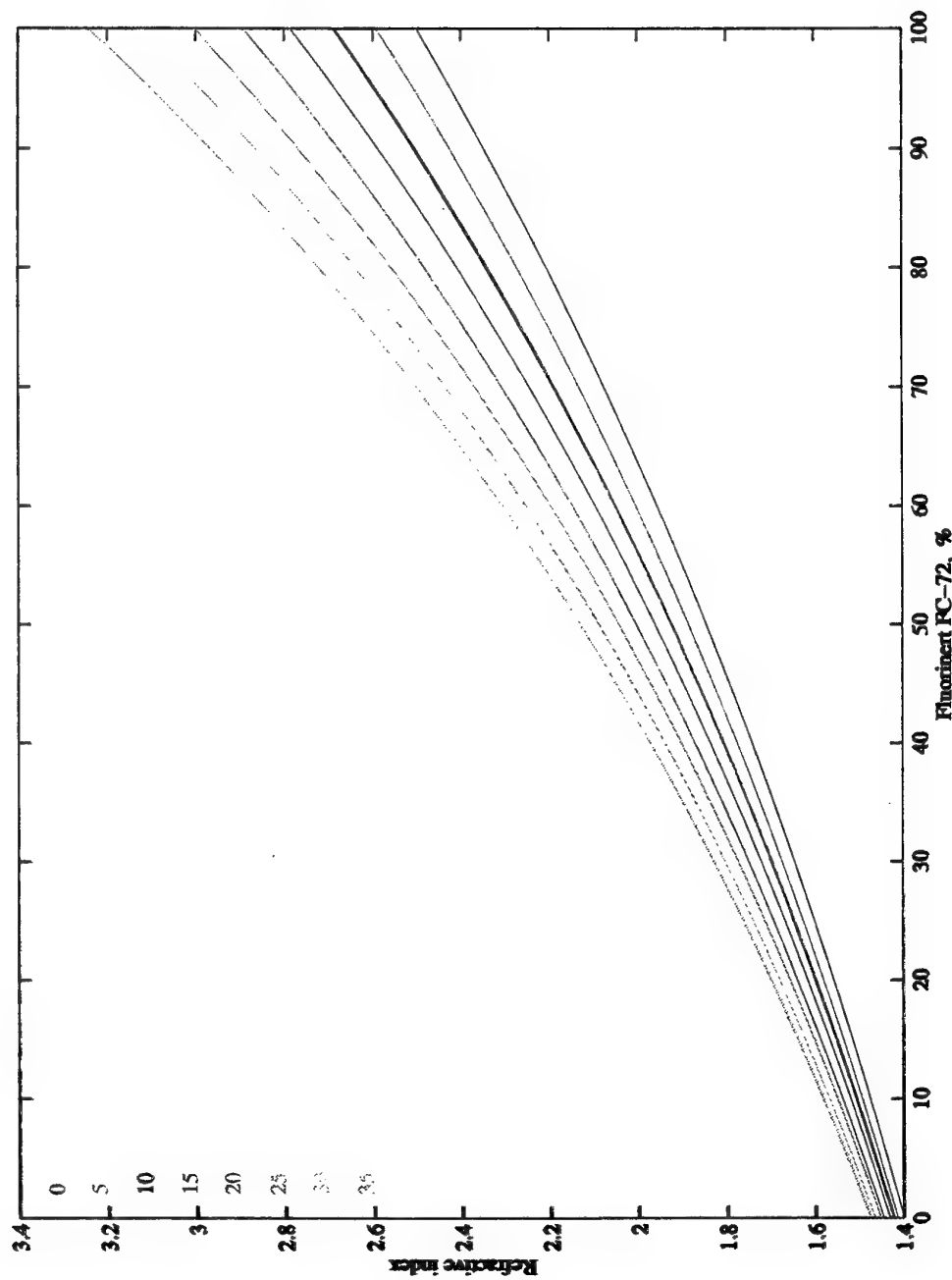


Figure 17: Refractive index as a function of the percentage of Fluorinert FC-72™ in a Fluorinert FC-72™ - n-hexane mixture, when the mixture and exterior water of 35‰ salinity are maintained at temperatures of 0, 5, 10, 15, 20, 25, 30 and 35°C.

THIS PAGE LEFT INTENTIONALLY BLANK

Figs 18 and 19 show how the target strength alters for 100  $\mu$ s tone bursts of frequencies up to 450 kHz, for temperatures of 10, 20 and 30°C. Again the projector and receiver were located 1000 m from a 20 cm diameter stainless steel shell of 0.8 mm wall thickness in shallow depths of sea water of 35% salinity. In Fig. 18 the shell was filled with 68% Freon-113™ and 32% ethanol by volume; in Fig. 19 the liquids were 34% Fluorinert FC-72™ and 66% n-hexane by volume. Below 50 kHz temperature changes produce only a small change in the target strength, but for higher frequencies the changes get progressively larger, especially in going from 10 to 20°. Of course smaller temperature variations will alter the target strength by correspondingly less.

Fig. 20 compares the target strengths for 100  $\mu$ s tone bursts of frequencies to 450 kHz, for a 20 cm diameter stainless steel spherical shell of 0.8 mm wall thickness deployed at shallow depths in sea water of 20°C and 35% salinity. The filling fluids were 68% Freon-113™ and 32% ethanol by volume, 34% Fluorinert FC-72™ and 66% n-hexane by volume, air of 50% relative humidity, and water of 35% salinity. The target strength for the air-filled sphere is fairly constant and in close agreement to the formula for specular reflection from a sphere whose size is large compared to the wavelength, viz.

$$TS = 10 \log \frac{b^2}{4}. \quad (86)$$

Above 100 kHz the target strength of the water-filled sphere shows periodic changes of about 10 dB, with a period in the frequency domain of approximately 90 kHz. In general the values are higher than for the air-filled sphere. However, the Freon-113™ - ethanol and Fluorinert FC-72™ - n-hexane filled spheres have even larger target strengths, which vary relatively smoothly with frequency. In comparison to the air-filled sphere, there is a gain in excess of 10 dB in target strength at all frequencies studied. As noted previously, the performance of the two pairs of liquid combinations is similar, but not identical.

Although the theory developed is not restricted to the far field, the results of Fig. 7 to 20 were based on the projector and receiver being 1000 m from the centre of the sphere. Keeping the projector 1000 m from the centre of the sphere, but varying the distance of the receiver out along the axis from the centre of the sphere towards the projector, Fig. 21 shows the variation in apparent target strength for a 20 cm diameter stainless steel shell of 0.8 mm wall thickness deployed at shallow depths in sea water of 20°C and 35% salinity when filled with 34% Fluorinert FC-72™ and 66% n-hexane by volume. At 100, 200, 300 and 400 kHz the farfield condition

$$\frac{(2b)^2}{\lambda_{L,1}} \quad (87)$$

is satisfied at approximately 2.7, 5.3, 8 and 10.7 m, respectively. Examination of the curves in Fig. 21 shows constancy of the apparent target strength occurs at ranges slightly beyond these at the respective frequencies. Below approximately 200 kHz, the

apparent target strength increases with range; at higher frequencies it generally decreases with range.

Figs 7 to 21 have shown intensities in the frequency domain. Figs 22 to 25 show the reflected signal in the time domain, where 0 ms corresponds to the arrival of the first portion of the reflected signal at the receiver. The pressure is relative to a value of 1 at the projector. In each diagram the waves impinge upon a 20 cm diameter stainless steel shell of 0.8 mm wall thickness deployed at shallow depths in sea water of 20°C and 35‰ salinity filled with 68% Freon-113™ and 32% ethanol by volume. In Fig. 22 the signal emitted by the projector was a 200 kHz tone burst of 100  $\mu$ s duration. The most intense signal corresponds to the focused reflection from the rear of the sphere, which arrives 0.44 ms after the front surface specular reflection. Subsequent reflections are related to multiple internal reflections within the sphere. Fig. 23 shows the equivalent signal for a tone burst lasting 500  $\mu$ s. Due to the long duration of the tone burst there is overlap of signals returning from different parts of the sphere, but that from the rear surface still dominates.

In Figs 24 and 25 a chirped signal of 10 kHz bandwidth centred on 200 kHz was used. In Fig. 24 the duration of the chirp was 100  $\mu$ s and although the signal from the rear surface dominates, a later multiply-reflected signal is almost as large. Fig. 25 shows that a 500  $\mu$ s chirp results in much interference of returns from different parts of the sphere. The first rear surface reflection and a somewhat later multiply-reflected signal are the most prominent returns.

## 6. Conclusions

Selection of the appropriate materials to make a fluid-filled spherical shell target of a required target strength is no easy matter, for not only is the target strength sensitive to a number of material parameters, but with a given selection of materials, the target strength is sensitive to both the form of the incoming sound waves and the environment.

Consider first the incoming sound waves. Fig. 7 shows that the target strength varies greatly for small changes in the frequency if continuous waves are used. Experimentally the implication is that drift in the frequency will lead to a large change in the target strength. Fortunately, these variations can be largely eliminated by the use of pulsed signals, which effectively average over many frequencies. However, there are some target strength variations with pulse length below about 50 kHz, or in the region of oscillatory target strength behaviour.

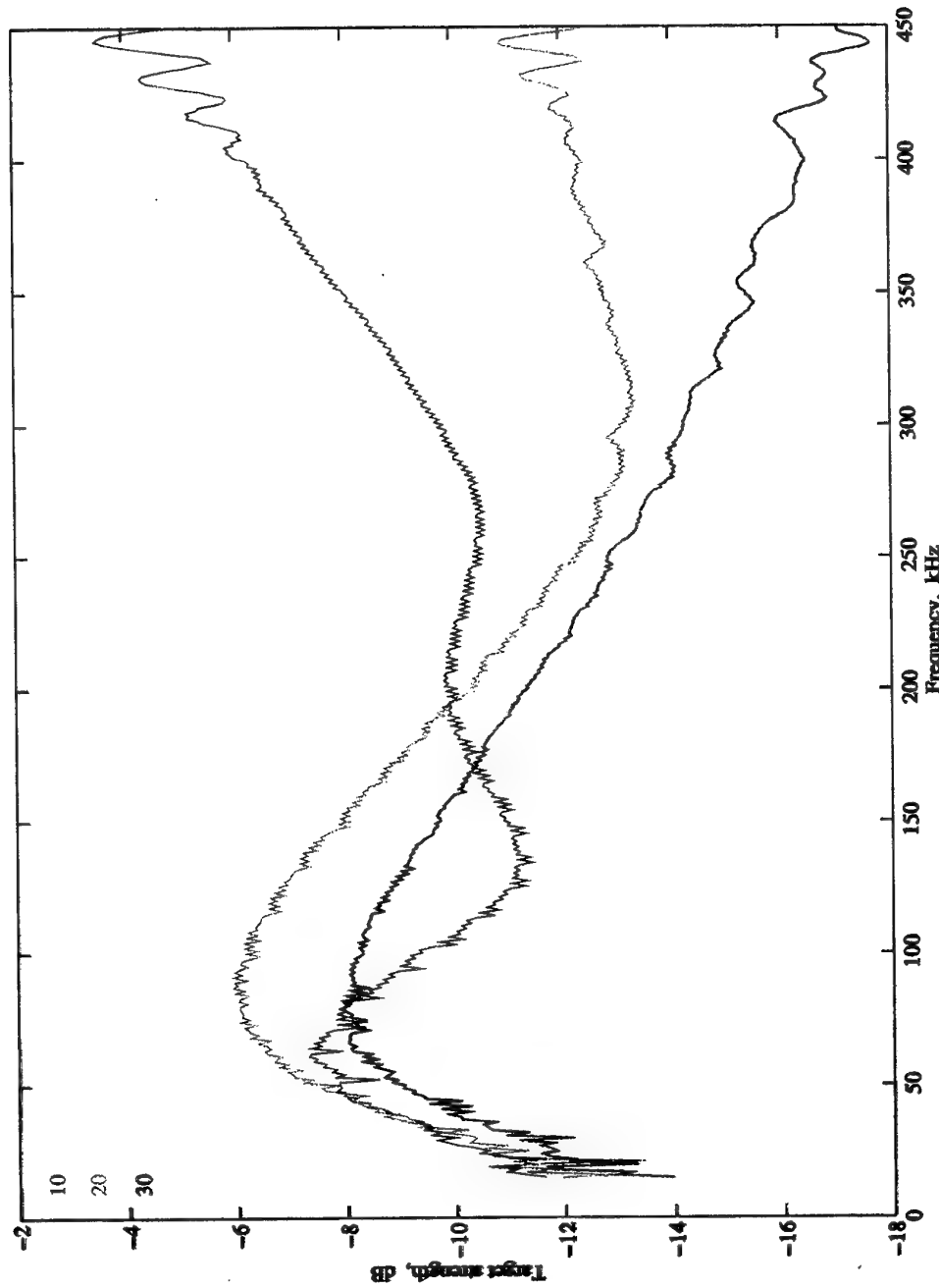


Figure 18: Variation of target strength with temperature for a stainless steel spherical shell of 20 cm diameter and 0.8 mm wall thickness filled with 68% Fream-113™ and 32% ethanol by volume and deployed at shallow depths in sea water of 35‰ salinity at 10, 20 and 30°C. The incoming waves are 100  $\mu$ s tone bursts.

THIS PAGE LEFT INTENTIONALLY BLANK

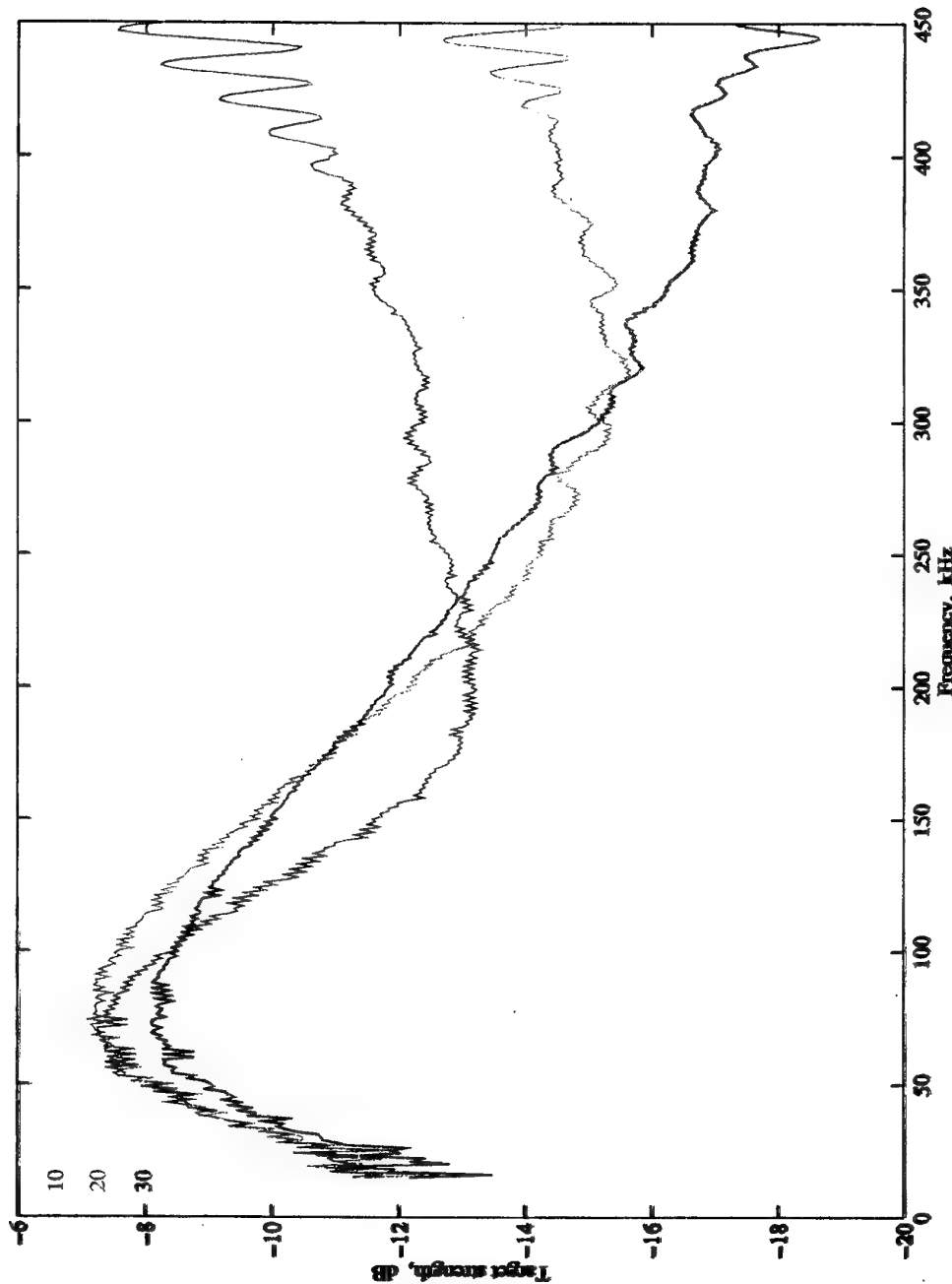


Figure 19: Variation of target strength with temperature for a stainless steel spherical shell of 20 cm diameter and 0.8 mm wall thickness filled with 34% Fluonvert FC-772™ and 66% n-hexane by volume and deployed at shallow depths in sea water of 35‰ salinity at 10, 20 and 30°C. The incoming waves are 100  $\mu$ s tone bursts.

THIS PAGE LEFT INTENTIONALLY BLANK

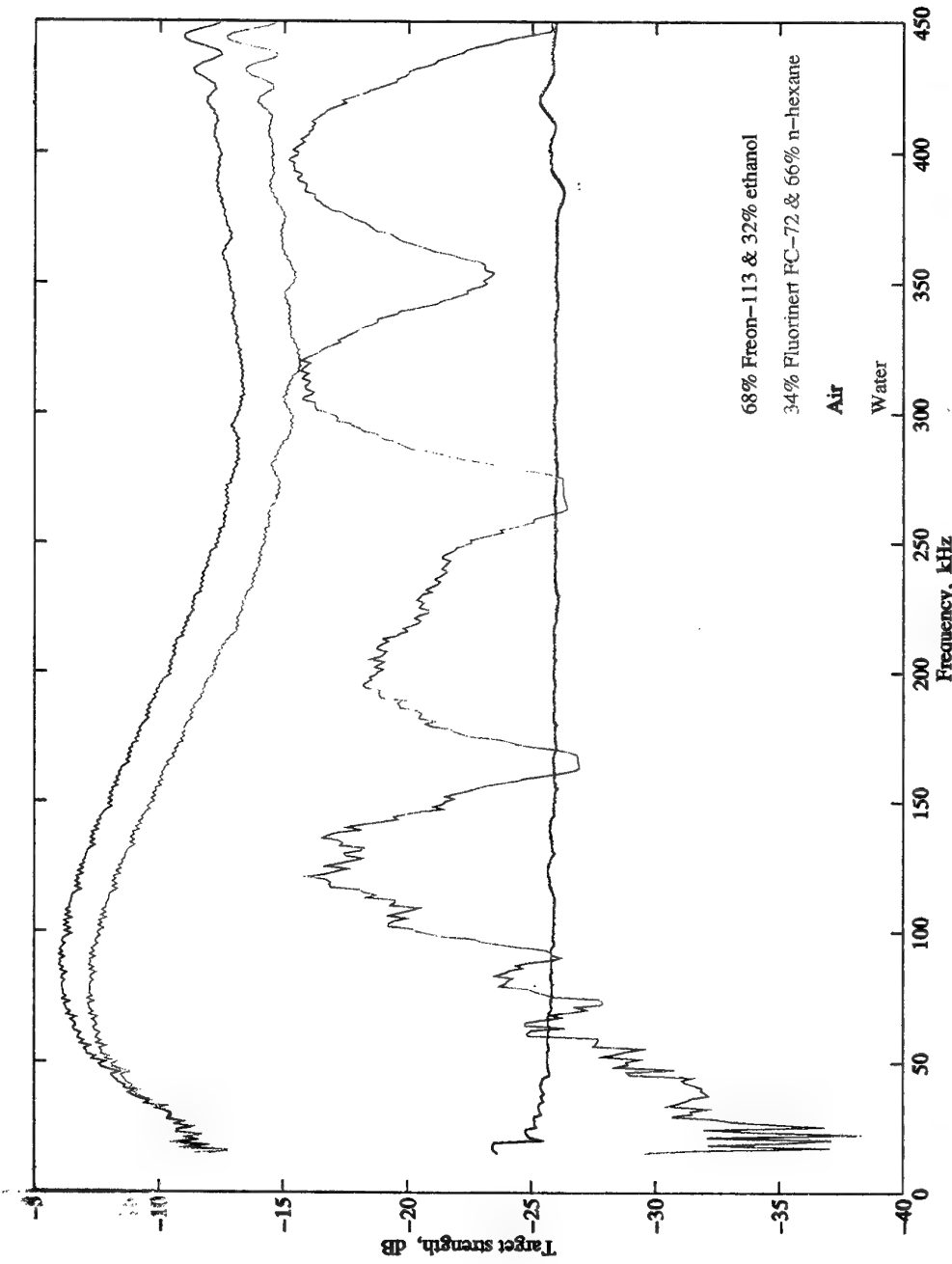


Figure 20: Efficacy of filling fluids: Target strength of a stainless steel spherical shell of 20 cm diameter and 0.8 mm wall thickness deployed at shallow depths in sea water of 20°C and 35% salinity. The incoming waves are 100  $\mu$ s tone bursts and the filling fluids are 68% Freon-113™ and 32% ethanol by volume, 34% Fluorinert FC-72™ and 66% n-hexane by volume, air of 50% relative humidity and sea water of 35% salinity.

THIS PAGE LEFT INTENTIONALLY BLANK

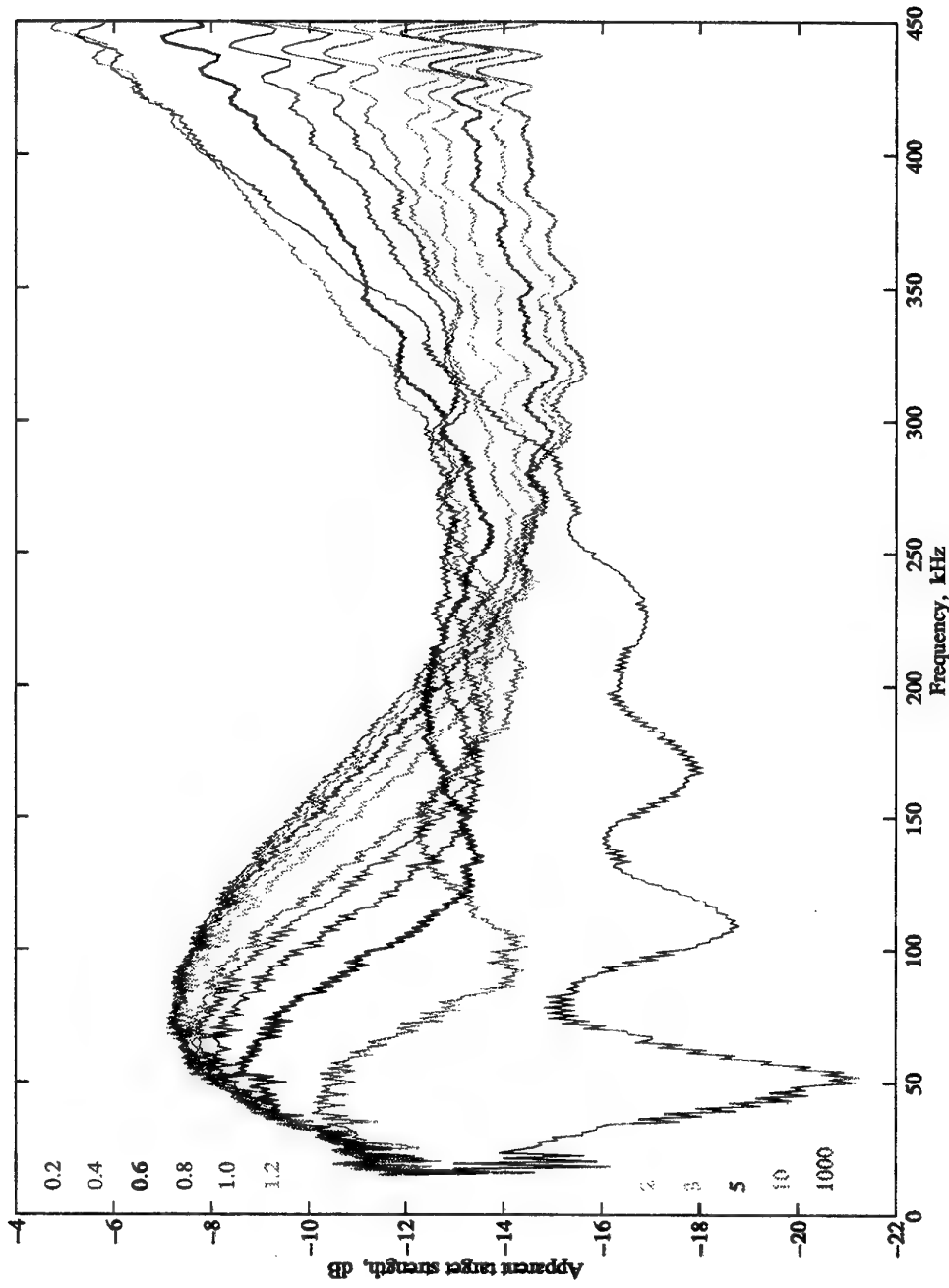


Figure 21: Variation of apparent target strength with receiver range for a stainless steel spherical shell of 20 cm diameter and 0.8 mm wall thickness filled with 34% Fluorinert FC-72™ and 66% *n*-hexane by volume and deployed at shallow depths in sea water of 20°C and 35‰ salinity. The projector is 1000 m from the centre of the sphere and emits 100  $\mu$ s tone bursts. The receiver is on the axis from the centre of the sphere to the projector and is 0.2, 0.4, 0.6, 0.8, 1.0, 1.2, 2, 3, 5, 10 and 1000 m from the centre of the sphere.

THIS PAGE LEFT INTENTIONALLY BLANK

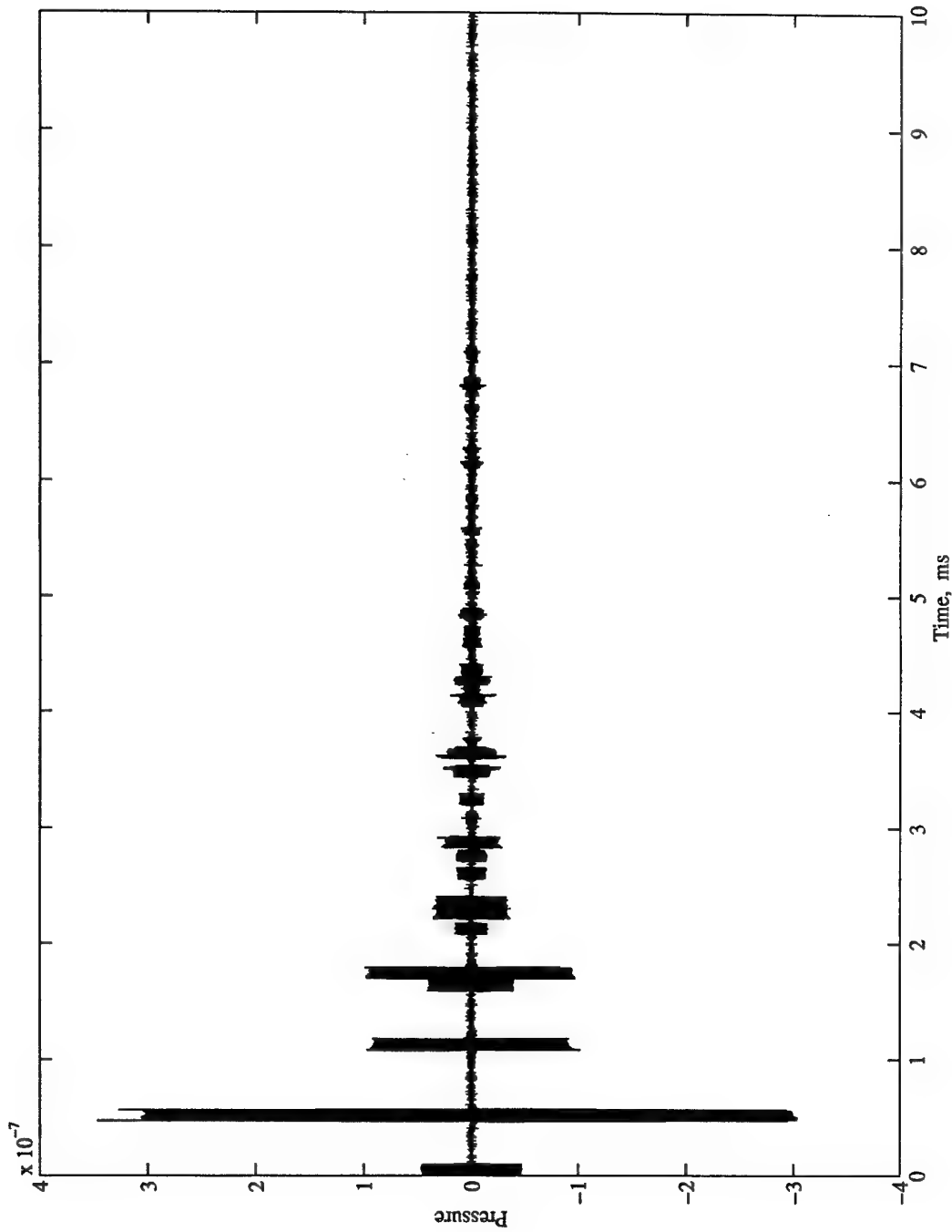


Figure 22: The reflected signal arriving at a receiver co-located with a projector 1000 m from a stainless steel spherical shell of 20 cm diameter and 0.8 mm wall thickness filled with 68% Freon-113™ and 32% ethanol by volume and deployed at shallow depths in sea water of 20°C and 35‰ salinity. The projector emitted a 100  $\mu$ s tone burst of 200 kHz, and 0 ms corresponds to the arrival of the first part of the return signal.

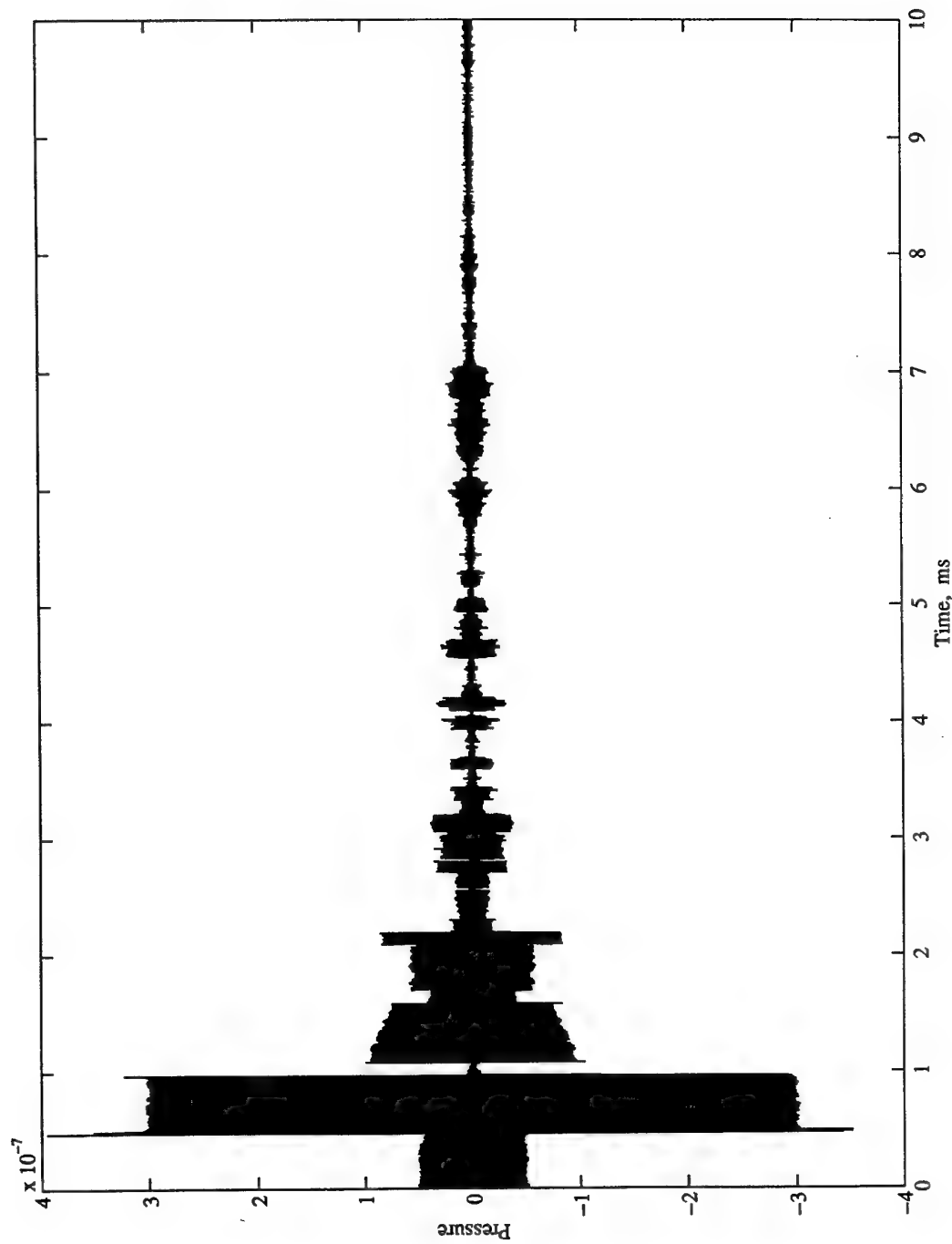


Figure 23: The reflected signal arriving at a receiver co-located with a projector 1000 m from a stainless steel spherical shell of 20 cm diameter and 0.8 mm wall thickness filled with 68% Freon-113™ and 32% ethanol by volume and deployed at shallow depths in sea water of 20°C and 35‰ salinity. The projector emitted a 500  $\mu$ s tone burst of 200 kHz, and 0 ms corresponds to the arrival of the first part of the return signal.

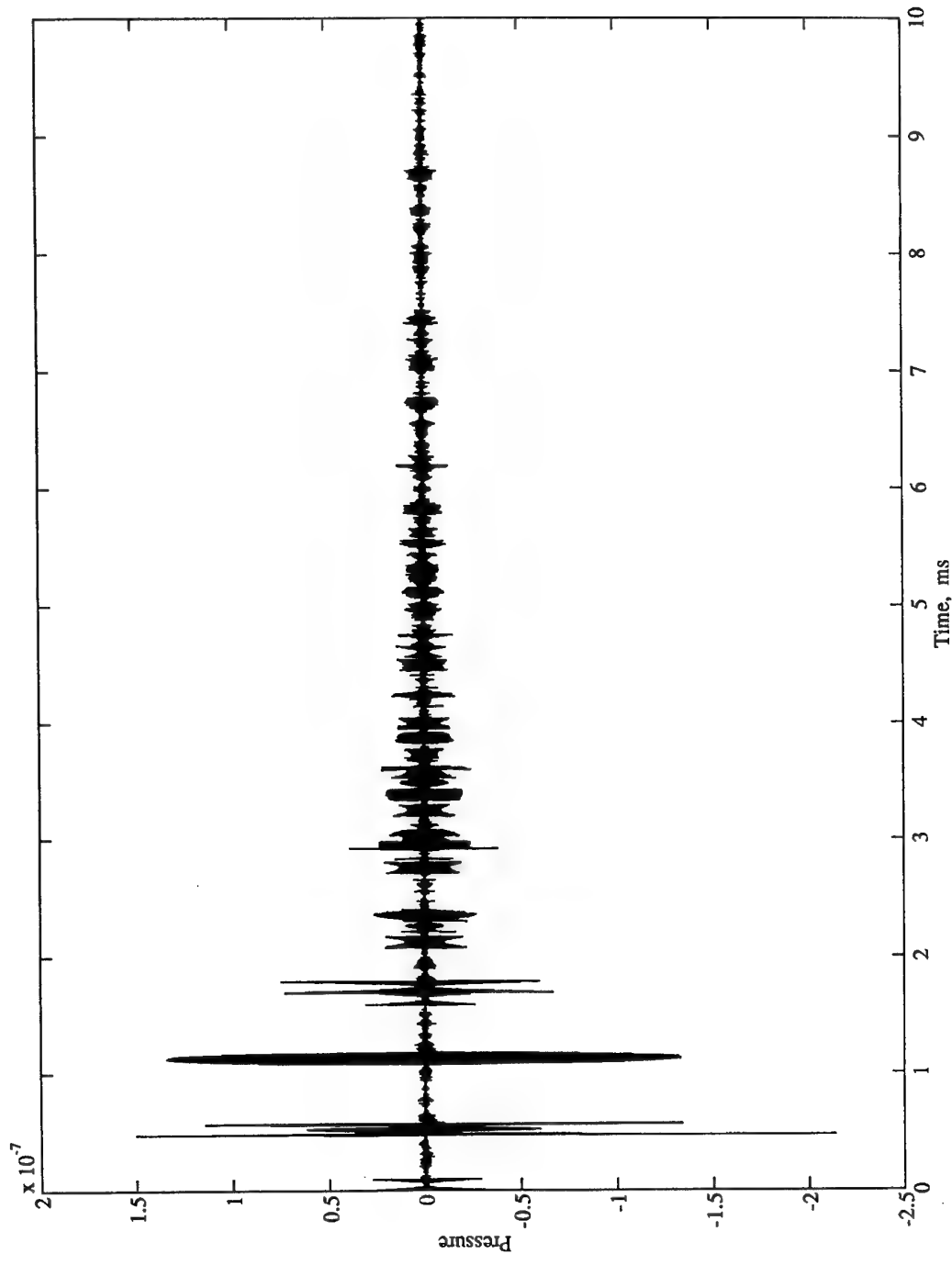


Figure 24: The reflected signal arriving at a receiver co-located with a projector 1000 m from a stainless steel spherical shell of 20 cm diameter and 0.8 mm wall thickness filled with 68% Freon-113™ and 32% ethanol by volume and deployed at shallow depths in sea water of 20°C and 35‰ salinity. The projector emitted a 10 kHz bandwidth chirp centred on 200 kHz and of 100  $\mu$ s duration, and 0 ms corresponds to the arrival of the first part of the return signal.

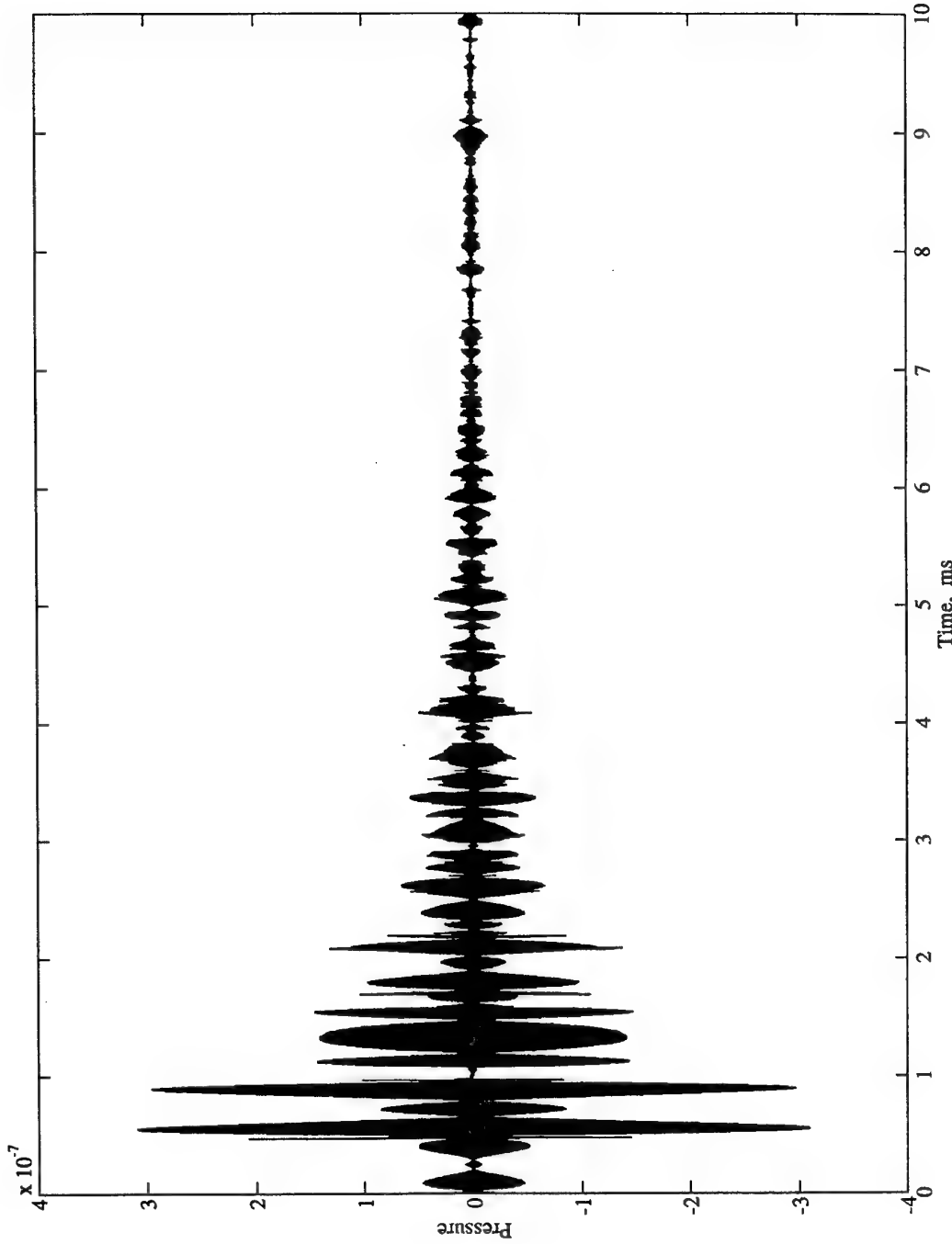


Figure 25: The reflected signal arriving at a receiver co-located with a projector 1000 m from a stainless steel spherical shell of 20 cm diameter and 0.8 mm wall thickness filled with 68% Freon-113™ and 32% ethanol by volume and deployed at shallow depths in sea water of 20°C and 35‰ salinity. The projector emitted a 10 kHz bandwidth chirp centred on 200 kHz and of 500  $\mu$ s duration, and 0 ms corresponds to the arrival of the first part of the return signal.

Now consider the material parameters which will lead to a large target strength above 100 kHz. A shell of aluminium or pyrex glass would optimise the target strength, but as these are soft or brittle materials, stainless steel might be preferable as it is more robust. As might be expected, increasing the diameter of the sphere will give a larger target strength. A thin shell wall will also lead to a large target strength, but may be too difficult to manufacture and will be easily damaged. A thickness of 0.8 mm might be classed as a reasonable compromise. Figs 14 and 15 indicate that the target strength is quite sensitive to the thickness, so variations in the wall thickness need to be avoided. In particular, a sphere made by welding together two spun hemispheres is not appropriate, as the process of spinning leads to a variable wall thickness.

Choice of the optimum combination of fluids with which to fill the shell depends on the temperature. Variations of a few degrees will make only a modest change to the target strength, but a combination chosen for warm waters, say off northern Australia, will behave quite differently in cool waters off southern Australia. For frequencies below 200 kHz a mixture of Freon-113™ and ethanol, or Fluorinert FC-72™ and n-hexane will work quite well if the ratio of liquids is chosen to give a refractive index between 1.8 and 1.9. At frequencies above 250 kHz the same liquids mixed to give a refractive index between 1.6 and 1.7 will produce high target strengths.

In general, a well selected fluid-filled sphere can give a large target strength, but it will be somewhat sensitive to temperature and hence refractive index of the filling fluids. Consequently, the water temperature at the site at which it is to be used should be measured so the target strength can be calculated. Better still, the target strength should actually be measured at the site.

If it is difficult to manufacture a shell with a uniform wall thickness, consideration could be given to spherical shells composed of rubber-coated metals or non-metallic materials, such as plastics. It is possible that the target strengths may be less sensitive to variations in their shell parameters. Because of their significant viscosity, the above theory is not valid, so they were not compared in this study. The required theory is an extension of that presented here.

## 7. References

Abramowitz, M., and Stegun, I.A. (Ed.). (1965). *Handbook of mathematical functions with formulas, graphs and mathematical tables*. New York: Dover Publications.

Faran, J.F., Jr. (1951). Sound scattering by solid cylinders and spheres. *Journal of the Acoustical Society of America*, **23**, 405-418.

Francois, R.E., and Garrison, G.R. (1982). Sound absorption based on ocean measurements: part II: boric acid contribution and equation for total absorption. *Journal of the Acoustical Society of America*, **72**, 1879-1890.

Gautschi, W. (1967). Computational aspects of three-term recurrence relations. *SIAM Review*, **9**, 24-82.

Goodman, R.R., and Stern, R. (1962). Reflection and transmission of sound by elastic spherical shells. *Journal of the Acoustical Society of America*, **34**, 338-344.

Gray, D.W. (Ed.). (1972). *American Institute of Physics handbook* (3rd ed.). New York: McGraw-Hill Book Company.

Harris, C.M. (1971). Effects of humidity on the velocity of sound in air. *Journal of the Acoustical Society of America*, **49**, 890-893.

Hickling, R. (1964). Analysis of echoes from a hollow metallic sphere in water. *Journal of the Acoustical Society of America*, **36**, 1124-1137.

Junger, M.C. (1952). Sound scattering by thin elastic shells. *Journal of the Acoustical Society of America*, **24**, 366-373.

Kaye, G.W.C. and Laby, T.H. (1973). *Tables of physical and chemical constants and some mathematical functions* (14th ed.). London: Longman.

Kneser, H.O. (1931). Zur Dispersionstheorie des Schalles. *Ann. Physik (Leipzig)*, **11**, 761-776.

Leader, G.R., Fainberg, A.H., Atwell, R.L., and Soulen, J.R. (1969). *Fluids for acoustic lenses*. King of Prussia, PA: Pennwalt Corporation Research and Development Department. (NTIS No. AD-861-195).

Miller, D.C. (1937). *Sound waves, their shape and speed*. New York: Macmillan.

Millero, F.J., and Poisson, A. (1981). International one-atmosphere equation of state of seawater. *Deep Sea Research*, **28A(6)**, 625-629.

Morse, P.M. (1936). *Vibration and sound*. New York: McGraw-Hill Book Company.

Morse, P.M., and Feshbach, H. (1953). *Methods of theoretical physics, parts I and II*. New York: McGraw-Hill Book Company.

Morse, P.M., and Ingard, K.U. (1968). *Theoretical acoustics*. New York: McGraw-Hill Book Company.

Olver, F.W.J., and Sookne, D.J. (1972). Note on backward recurrence algorithms. *Mathematics of Computation*, **26**, 941-947.

Piercy, J.E. (1969). Role of the vibrational relaxation of nitrogen in the absorption of sound in air. *Journal of the Acoustical Society of America*, **46**, 602-604.

Rayleigh, Lord (1945). *The theory of sound*. New York: Dover Publications.

3M [199-]. *Fluorinert™ Liquids, Product Manual*. [St Paul, MN: 3M Industrial Chemical Products Division].

Timmermans, J. (1950). *Physico-chemical constants of pure organic compounds*. New York: Elsevier Publishing Company.

## Appendix A

To solve for  $P$  in equation (6) the spherical coordinates

$$x = r \sin \theta \cos \phi \quad (A1)$$

$$y = r \sin \theta \sin \phi \quad (A2)$$

$$z = r \cos \theta \quad (A3)$$

are used and it is noted that  $P$  has no  $\phi$  dependence. Hence equation (16) can be rewritten as

$$\frac{1}{r^2} \frac{\partial}{\partial r} \left( r^2 \frac{\partial P}{\partial r} \right) + \frac{1}{r^2 \sin \theta} \frac{\partial}{\partial \theta} \left( \sin \theta \frac{\partial P}{\partial \theta} \right) = \frac{1}{c_{L,i}^2} \frac{\partial^2 P}{\partial t^2}. \quad (A4)$$

Solution of equation (A4) proceeds by separating out the time and position dependence of  $P$  as

$$P = p(r, \theta).T(t) \quad (A5)$$

and substituting this into equation (A4). Hence

$$\frac{1}{r^2 p} \frac{\partial}{\partial r} \left( r^2 \frac{\partial p}{\partial r} \right) + \frac{1}{p r^2 \sin \theta} \frac{\partial}{\partial \theta} \left( \sin \theta \frac{\partial p}{\partial \theta} \right) = \frac{1}{c_{L,i}^2 T} \frac{\partial^2 T}{\partial t^2}. \quad (A6)$$

The left and right hand sides of equation (A6) are independent and can now be set equal to a constant  $-k_{L,i}^2$ , so the right hand side becomes

$$\frac{d^2 T}{dt^2} + k_{L,i}^2 c_{L,i}^2 T = 0 \quad (A7)$$

for which the solution is

$$T = e^{-ik_{L,i}c_{L,i}t} = e^{-i2\pi ft}. \quad (A8)$$

From the left hand side of equation (A6),

$$\frac{1}{r^2} \frac{\partial}{\partial r} \left( r^2 \frac{\partial p}{\partial r} \right) + \frac{1}{r^2 \sin \theta} \frac{\partial}{\partial \theta} \left( \sin \theta \frac{\partial p}{\partial \theta} \right) + k_{L,i}^2 p = 0 \quad (A9)$$

which can be solved by a separation of variables. Substituting

$$p(r, \theta) = R(r).Y(\theta) \quad (A10)$$

into equation (A9) yields

$$\frac{1}{R} \frac{d}{dr} \left( r^2 \frac{dR}{dr} \right) + k_{L,i}^2 r^2 = - \frac{1}{Y \sin \theta} \frac{d}{d\theta} \left( \sin \theta \frac{dY}{d\theta} \right). \quad (\text{A11})$$

Again the left and right hand sides of equation (A11) are independent and are set equal to  $l(l+1)$ . The right hand side becomes

$$\frac{1}{\sin \theta} \left[ \cos \theta \frac{dY}{d\theta} + \sin \theta \frac{d^2 Y}{d\theta^2} \right] + l(l+1)Y = 0. \quad (\text{A12})$$

which can be solved by making the substitution  $\eta = \cos \theta$  and noting that

$$\sin \theta = (1 - \eta^2)^{1/2} \quad (\text{A13})$$

$$\frac{d\eta}{d\theta} = -\sin \theta \quad (\text{A14})$$

$$\frac{d^2 \eta}{d\theta^2} = -\cos \theta = -\eta \quad (\text{A15})$$

$$\frac{dY}{d\theta} = \frac{dY}{d\eta} \frac{d\eta}{d\theta} \quad (\text{A16})$$

$$= -\sin \theta \frac{dY}{d\eta} = -(1 - \eta^2)^{1/2} \frac{dY}{d\eta} \quad (\text{A17})$$

$$\frac{d^2 Y}{d\theta^2} = \frac{d}{d\theta} \left( \frac{dY}{d\eta} \frac{d\eta}{d\theta} \right) \quad (\text{A18})$$

$$= \frac{d^2 Y}{d\eta^2} \left( \frac{d\eta}{d\theta} \right)^2 + \frac{d^2 \eta}{d\theta^2} \frac{dY}{d\eta} \quad (\text{A19})$$

$$= (1 - \eta^2) \frac{d^2 Y}{d\eta^2} - \eta \frac{dY}{d\eta} \quad (\text{A20})$$

Substitution into (A12) gives Legendre's equation

$$(1-\eta^2) \frac{d^2Y}{d\eta^2} - 2\eta \frac{dY}{d\eta} + l(l+1)Y = 0 \quad (\text{A21})$$

The only solutions which are finite across the range  $\eta = [-1, 1]$  occur for  $l = 0, 1, 2, \dots$ . These are the Legendre polynomials

$$Y = P_l(\eta) = P_l(\cos \theta). \quad (\text{A22})$$

The left hand side of equation (A11) can be expressed as

$$2r \frac{dR}{dr} + r^2 \frac{d^2R}{dr^2} + [k_{L,i}^2 r^2 - l(l+1)]R = 0 \quad (\text{A23})$$

which after substitution of  $\zeta = k_{L,i}r$  and using

$$\frac{d\zeta}{dr} = k_{L,i} \quad (\text{A24})$$

$$\frac{dR}{dr} = \frac{dR}{d\zeta} \frac{d\zeta}{dr} = k_{L,i} \frac{dR}{d\zeta} \quad (\text{A25})$$

$$\frac{d^2R}{dr^2} = \frac{d}{d\zeta} \left( \frac{dR}{d\zeta} \frac{d\zeta}{dr} \right) \frac{d\zeta}{dr} \quad (\text{A26})$$

$$= k_{L,i}^2 \frac{d^2R}{d\zeta^2} \quad (\text{A27})$$

can be rewritten as

$$\frac{d^2R}{d\zeta^2} + \frac{2}{\zeta} \frac{dR}{d\zeta} + [\zeta^2 - l(l+1)] \frac{R}{\zeta^2} = 0 \quad (\text{A28})$$

for which the possible outward going wave solutions are  $j_l(\zeta)$ ,  $n_l(\zeta)$ , or  $h_l(\zeta)$  (Morse and Feshbach, 1953, p. 1465; Morse and Ingard, 1968, p. 337). These are the spherical Bessel, Neumann and Hankel functions of order  $l$ , respectively. The spherical Hankel function is related to the other two functions via

$$h_l = j_l + i n_l. \quad (\text{A29})$$

In the internal fluid the range, and hence  $\zeta$ , can fall to zero, at which stage  $n_l(\zeta)$  and  $h_l(\zeta)$  are unbounded. Thus the only valid solution is  $j_l(\zeta)$ . On the other hand, in the external fluid where the range, and hence  $\zeta$ , can approach infinity,  $h_l(\zeta)$  is a valid solution. Consequently, in the two media

$$p_1 = \sum_{l=0}^{\infty} P_l(\cos \theta_r) A_l h_l(k_{L,1} r_r) \quad (A30)$$

and

$$p_3 = \sum_{l=0}^{\infty} P_l(\cos \theta_r) B_l j_l(k_{L,3} r_r) \quad (A31)$$

## Appendix B

To solve for  $\vec{A}$  in equation (22) it is first noted that

$$\vec{A} = (0, 0, A_\phi). \quad (B1)$$

Hence,

$$\vec{\nabla} \times \vec{A} = \left[ \frac{1}{r \sin \theta} \frac{d}{d\theta} (A_\phi \sin \theta) \right] \vec{r} - \left[ \frac{1}{r} \frac{\partial}{\partial r} (r A_\phi) \right] \vec{\theta} \quad (B2)$$

and

$$\begin{aligned} \vec{\nabla} \times \vec{\nabla} \times \vec{A} &= \frac{1}{r^2 \sin \theta} \frac{\partial}{\partial \phi} \left[ \frac{\partial}{\partial r} (r A_\phi) \right] \vec{r} + \frac{1}{r \sin \theta} \frac{\partial}{\partial \phi} \left[ \frac{1}{r \sin \theta} \frac{\partial}{\partial \theta} (A_\phi \sin \theta) \right] \vec{\theta} \\ &+ \frac{1}{r} \left\{ \frac{\partial}{\partial r} \left[ -\frac{\partial}{\partial r} (r A_\phi) \right] - \frac{\partial}{\partial \theta} \left[ \frac{1}{r \sin \theta} \frac{\partial}{\partial \theta} (A_\phi \sin \theta) \right] \right\} \vec{\phi} \end{aligned} \quad (B3)$$

where  $\vec{r}$ ,  $\vec{\theta}$  and  $\vec{\phi}$  are the unit vectors in the spherical coordinate system. Substitution of equation (B3) into equation (22) gives

$$\frac{1}{c_T^2} \frac{\partial^2 A_\phi}{\partial t^2} = \frac{1}{r} \frac{\partial^2}{\partial r^2} (r A_\phi) + \frac{1}{r^2} \frac{\partial}{\partial \theta} \left[ \frac{1}{\sin \theta} \frac{\partial}{\partial \theta} (A_\phi \sin \theta) \right] \quad (B4)$$

Solution of equation (B4) is again achieved through a separation of variables,

$$A_\phi = \alpha_\phi(r, \theta, \phi) \cdot T(t) \quad (B5)$$

which gives

$$\frac{1}{c_T^2 T} \frac{d^2 T}{dt^2} = \frac{1}{\alpha_\phi r} \frac{\partial^2}{\partial r^2} (r \alpha_\phi) + \frac{1}{\alpha_\phi r^2} \frac{\partial}{\partial \theta} \left[ \frac{1}{\sin \theta} \frac{\partial}{\partial \theta} (\alpha_\phi \sin \theta) \right]. \quad (B6)$$

Both sides of equation (B6) are independent and are set equal to  $-k_T^2$ . Thus the left hand side becomes

$$\frac{d^2 T}{dt^2} + k_T^2 c_T^2 T = 0 \quad (B7)$$

the solution of which is

$$T = e^{-ik_T c_T t}. \quad (B8)$$

The right hand side of equation (B6) becomes

$$0 = \frac{1}{r^2} \frac{\partial}{\partial r} \left( r^2 \frac{\partial \alpha_\phi}{\partial r} \right) + \frac{1}{r^2} \frac{\partial}{\partial \theta} \left[ \frac{1}{\sin \theta} \frac{\partial}{\partial \theta} (\alpha_\phi \sin \theta) \right] + k_T^2 \alpha_\phi \quad (B9)$$

which is solved by a further separation of variables into

$$\alpha_\phi = X(r) \cdot Z(\theta) \quad (B10)$$

to give

$$\frac{1}{X} \frac{\partial}{\partial r} \left( r^2 \frac{\partial X}{\partial r} \right) + k_T^2 r^2 = - \frac{1}{Z} \frac{\partial}{\partial \theta} \left[ \frac{1}{\sin \theta} \frac{\partial}{\partial \theta} (Z \sin \theta) \right]. \quad (B11)$$

Again both sides of equation (B11) are independent and are set equal to  $l(l+1)$ . From the left hand side,

$$\frac{d}{dr} \left( r^2 \frac{dX}{dr} \right) + k_T^2 r^2 X = l(l+1)X \quad (B12)$$

for which the solution is

$$X = G_l j_l(k_T r) + H_l n_l(k_T r) \quad (B13)$$

since  $A_\phi$  applies to medium 2, which has bounds not equal to 0 or  $\infty$ . The right hand side of equation (B11) gives, after some simplification,

$$0 = \frac{d^2 Z}{d\theta^2} + \cot \theta \frac{dZ}{d\theta} + \left[ l(l+1) - \frac{1}{\sin^2 \theta} \right] Z \quad (B14)$$

for which the solution is

$$Z = \frac{\partial}{\partial \theta} P_l(\cos \theta). \quad (B15)$$

Hence,

$$\alpha_\phi = \sum_{l=0}^{\infty} \frac{\partial}{\partial \theta} P_l(\cos \theta) [G_l j_l(k_T r) + H_l n_l(k_T r)] \quad (B16)$$

## Appendix C

The coefficients required to calculate  $C_l$  and  $D_l$  from equations (40) and (41) are

$$\gamma_{11} = \frac{\sigma}{1-2\sigma} (k_{L,2}b)^2 j_l(k_{L,2}b) - (k_{L,2}b)^2 j_l''(k_{L,2}b) \quad (C1)$$

$$\gamma_{12} = \frac{\sigma}{1-2\sigma} (k_{L,2}b)^2 n_l(k_{L,2}b) - (k_{L,2}b)^2 n_l''(k_{L,2}b) \quad (C2)$$

$$\gamma_{13} = l(l+1)j_l(k_T b) - l(l+1)k_T b j_l'(k_T b) \quad (C3)$$

$$\gamma_{14} = l(l+1)n_l(k_T b) - l(l+1)k_T b n_l'(k_T b) \quad (C4)$$

$$\gamma_{15} = \frac{(k_T b)^2}{2\rho_2} h_l^*(k_{L,1}b) \quad (C5)$$

$$g_1 = \frac{(k_T b)^2}{2\rho_2} j_l(k_{L,1}b) \quad (C6)$$

$$\gamma_{21} = \frac{\sigma}{1-2\sigma} (k_{L,2}a)^2 j_l(k_{L,2}a) - (k_{L,2}a)^2 j_l''(k_{L,2}a) \quad (C7)$$

$$\gamma_{22} = \frac{\sigma}{1-2\sigma} (k_{L,2}a)^2 n_l(k_{L,2}a) - (k_{L,2}a)^2 n_l''(k_{L,2}a) \quad (C8)$$

$$\gamma_{23} = l(l+1)j_l(k_T a) - l(l+1)k_T a j_l'(k_T a) \quad (C9)$$

$$\gamma_{24} = l(l+1)n_l(k_T a) - l(l+1)k_T a n_l'(k_T a) \quad (C10)$$

$$\gamma_{26} = \frac{(k_T a)^2}{2\rho_2} j_l(k_{L,3}a) \quad (C11)$$

$$\gamma_{31} = k_{L,2} b j_l'(k_{L,2}b) \quad (C12)$$

$$\gamma_{32} = k_{L,2} b n_l'(k_{L,2}b) \quad (C13)$$

$$\gamma_{33} = l(l+1)j_l(k_T b) \quad (C14)$$

$$\gamma_{34} = l(l+1)n_l(k_T b) \quad (C15)$$

$$\gamma_{35} = \frac{k_{L,1}b}{\rho_1} h_l''(k_{L,1}b) \quad (C16)$$

$$g_3 = \frac{k_{L,1}b}{\rho_1} j_l'(k_{L,1}b) \quad (C17)$$

$$\gamma_{41} = k_{L,2}a j_l'(k_{L,2}a) \quad (C18)$$

$$\gamma_{42} = k_{L,2}a n_l'(k_{L,2}a) \quad (C19)$$

$$\gamma_{43} = l(l+1) j_l(k_T a) \quad (C20)$$

$$\gamma_{44} = l(l+1) n_l(k_T a) \quad (C21)$$

$$\gamma_{46} = \frac{k_{L,3}a}{\rho_3} j_l''(k_{L,3}a) \quad (C22)$$

$$\gamma_{51} = 2k_{L,2}b j_l'(k_{L,2}b) - 2 j_l(k_{L,2}b) \quad (C23)$$

$$\gamma_{52} = 2k_{L,2}b n_l'(k_{L,2}b) - 2 n_l(k_{L,2}b) \quad (C24)$$

$$\gamma_{53} = (k_T b) j_l''(k_T b) + [l(l+1)-2] j_l(k_T b) \quad (C25)$$

$$\gamma_{54} = (k_T b) n_l''(k_T b) + [l(l+1)-2] n_l(k_T b) \quad (C26)$$

$$\gamma_{61} = 2k_{L,2}a j_l'(k_{L,2}a) - 2 j_l(k_{L,2}a) \quad (C27)$$

$$\gamma_{62} = 2k_{L,2}a n_l'(k_{L,2}a) - 2 n_l(k_{L,2}a) \quad (C28)$$

$$\gamma_{63} = (k_T a) j_l''(k_T a) + [l(l+1)-2] j_l(k_T a) \quad (C29)$$

$$\gamma_{64} = (k_T a) n_l''(k_T a) + [l(l+1)-2] n_l(k_T a) \quad (C30)$$

The spherical Bessel, Neumann and Legendre functions and their derivatives needed to evaluate the above equations are listed in Appendix D.

## Appendix D

The spherical Bessel, Neumann and Legendre functions and their derivatives are commonly computed using the following recurrence relations:

$$j_l(z) = \begin{cases} \frac{\sin z}{z} & \text{for } l = 0 \\ \frac{\sin z}{z^2} - \frac{\cos z}{z} & \text{for } l = 1 \\ \frac{2l-1}{z} j_{l-1}(z) - j_{l-2}(z) & \text{for } l > 1 \end{cases} \quad (D1)$$

$$j'_l(z) = \begin{cases} \frac{\cos z}{z} - \frac{\sin z}{z^2} & \text{for } l = 0 \\ \frac{2}{z^2} \cos z + \left( \frac{1}{z} - \frac{2}{z^3} \right) \sin z & \text{for } l = 1 \\ (2l-1) \left[ \frac{j'_{l-1}(z)}{z} - \frac{j_{l-1}(z)}{z^2} \right] - j'_{l-2}(z) & \text{for } l > 1 \end{cases} \quad (D2)$$

$$j''_l(z) = \begin{cases} \left( \frac{2}{z^3} - \frac{1}{z} \right) \sin z - \frac{2}{z^2} \cos z & \text{for } l = 0 \\ \left( \frac{6}{z^4} - \frac{3}{z^2} \right) \sin z + \left( \frac{1}{z} - \frac{6}{z^3} \right) \cos z & \text{for } l = 1 \\ (2l-1) \left[ \frac{j''_{l-1}(z)}{z} - \frac{2j'_{l-1}(z)}{z^2} + \frac{2j_{l-1}(z)}{z^3} \right] - j''_{l-2}(z) & \text{for } l > 1 \end{cases} \quad (D3)$$

$$n_l(z) = \begin{cases} -\frac{\cos z}{z} & \text{for } l = 0 \\ -\frac{\sin z}{z} - \frac{\cos z}{z^2} & \text{for } l = 1 \\ \frac{2l-1}{z} n_{l-1}(z) - n_{l-2}(z) & \text{for } l > 1 \end{cases} \quad (D4)$$

$$n'_l(z) = \begin{cases} \frac{\sin z}{z} + \frac{\cos z}{z^2} & \text{for } l = 0 \\ \frac{2}{z^2} \sin z + \left( \frac{2}{z^3} - \frac{1}{z} \right) \cos z & \text{for } l = 1 \\ (2l-1) \left[ \frac{n'_{l-1}(z)}{z} - \frac{n_{l-1}(z)}{z^2} \right] - n'_{l-2}(z) & \text{for } l > 1 \end{cases} \quad (D5)$$

$$n_l''(z) = \begin{cases} \left(\frac{1}{z} - \frac{2}{z^3}\right) \cos z - \frac{2}{z^2} \sin z & \text{for } l=0 \\ \left(\frac{1}{z} - \frac{6}{z^3}\right) \sin z + \left(\frac{3}{z^2} - \frac{6}{z^4}\right) \cos z & \text{for } l=1 \\ (2l-1) \left[ \frac{n_{l-1}''(z)}{z} - \frac{2n_{l-1}'(z)}{z^2} + \frac{2n_{l-1}(z)}{z^3} \right] - n_{l-2}''(z) & \text{for } l>1 \end{cases} \quad (D6)$$

$$P_l(z) = \begin{cases} 1 & \text{for } l=0 \\ z & \text{for } l=1 \\ \frac{2l-1}{l} z P_{l-1}(z) - \frac{l-1}{l} P_{l-2}(z) & \text{for } l>1 \end{cases} \quad (D7)$$

For fixed  $z$  and varying  $l$  the behaviour of the spherical Bessel and Neumann functions is different in the ranges  $0 \leq l < z$  and  $z < l < \infty$ . The functions oscillate with slowly varying amplitude in the first range. In the second range the spherical Bessel function tends rapidly to zero, whereas the spherical Neumann function tends rapidly to  $-\infty$ . In this latter range the recursion relation of equation (D4) is stable, but that of equation (D1) is unstable and leads to increasing errors with increasing order. A further difficulty arises in calculating  $\sin(z)$  or  $\cos(z)$  when  $z$  approaches a zero of either trigonometric function. The rounding error associated in representing  $\pi$  in double precision is reflected in the result. The error may be amplified when  $z$  is both near a zero and large, as an imprecise value for  $\pi$  may be used in the argument reduction method needed for the sine and cosine routines. The procedures used to overcome these difficulties are outlined below.

The spherical Bessel function was calculated by one of three different methods, depending upon argument  $z$  and order  $l$ . For  $z < 10^{-4}$ , the ascending series (Abramowitz and Stegun 1965, p. 437)

$$j_l(z) = \frac{z^n}{1 \cdot 3 \cdot 5 \dots (2l+1)} \left[ 1 - \frac{\frac{1}{2} z^2}{1!(2l+3)} + \frac{\left(\frac{1}{2} z^2\right)^2}{2!(2l+3)(2l+5)} - \dots \right] \quad (D8)$$

was used.

For  $z > 25$  and  $l \leq z+1$ , an asymptotic expansion (Abramowitz and Stegun 1965, p. 437) was used to obtain the first two terms. The forward recursion formula of equation (D1) provided sufficient accuracy for higher order terms:

$$j_l(z) = \begin{cases} \frac{1}{z} \left\{ P\left(l + \frac{1}{2}, z\right) \sin\left[\zeta - \frac{l\pi}{2}\right] - Q\left(l + \frac{1}{2}, z\right) \cos\left[\zeta - \frac{l\pi}{2}\right] \right\} & \text{for } l = 0, 1 \\ \frac{2l-1}{z} j_{l-1}(z) - j_{l-2}(z) & \text{for } l > 1 \end{cases} \quad (\text{D9})$$

where

$$P\left(l + \frac{1}{2}, z\right) = \sum_{m=0}^{\left[\frac{1}{2}l\right]} (-1)^m \left(l + \frac{1}{2}, 2m\right) (2z)^{-2m} \quad (\text{D10})$$

$$Q\left(l + \frac{1}{2}, z\right) = \sum_{m=0}^{\left[\frac{1}{2}(l-1)\right]} (-1)^m \left(l + \frac{1}{2}, 2m+1\right) (2z)^{-2m-1} \quad (\text{D11})$$

$$\left(l + \frac{1}{2}, m\right) = \frac{(l+m)!}{m! \Gamma(l-k+1)} \quad (\text{D12})$$

and  $\zeta$  is a reduced sinusoidal argument related to  $z$  by

$$\zeta = z - \frac{201}{32} \times \text{round}\left(\frac{z}{2\pi}\right) - 0.001935307179586476925286767 \times \text{round}\left(\frac{z}{2\pi}\right) \quad (\text{D13})$$

For all other arguments and orders a method primarily attributed to J.C.P. Miller by Abramowitz and Stegun (1965, p. 452) was used:

$$j_l(z) = \iota J_l(z) \quad \text{for } l_m \leq l \leq l_{\max} \quad (\text{D14})$$

where  $\iota$  is a proportionality factor found by either

$$\iota = \frac{j_{l_m}(z)}{J_{l_m}(z)} \quad (\text{D15})$$

when  $j_{l_m}(z)$  is known, such as when the recursion is continued down to  $l_m = 0$ , or from

$$\iota = \frac{1}{\sqrt{\sum_{l=0}^{\infty} (2l+1) J_l^2(z)}} \quad (\text{D16})$$

In practice the summation in equation (D16) is continued up to  $l_{\max}$ . The  $J_l(z)$  terms are found for decreasing  $l$  via the recurrence relation

$$J_l(z) = \begin{cases} 0 & \text{for } l = l_{\max} + 1 \\ 1 & \text{for } l = l_{\max} \\ \frac{2l+3}{z} J_{l+1}(z) - J_{l+2}(z) & \text{for } l_m \leq l \leq l_{\max} - 1 \end{cases} . \quad (D17)$$

$l_{\max}$  needs to be chosen with some care. By trial and error it was found that provided  $l_{\max}$  satisfies

$$l_{\max} \leq 10^{2.1769 + 0.17527 \log z + 2.7941 \times 10^{-2} (\log z)^2 + 6.4446 \times 10^{-3} (\log z)^3 + 1.7055 \times 10^{-3} (\log z)^4} \quad (D18)$$

the backward recursion is stable down to  $l_m = 0$ . For larger values of  $l_{\max}$  the recursion is unstable.  $l_{\max}$  was usually obtained from equation (D18), which was always greater than the maximum  $l$  needed to evaluate equation (12). More computationally efficient methods are outlined by Gautschi (1967) and Olver and Sookne (1972).

Although equations (D2) and (D3) for the first and second derivatives of the spherical Bessel function do not diverge as quickly as equation (D1), inaccuracies in their evaluation do nevertheless occur when they are used, especially as the order increases. Better results were achieved by using

$$j'_l(z) = \frac{1}{2} \left[ j_{l-1}(z) - j_{l+1}(z) - \frac{j_l(z)}{z} \right] \quad (D19)$$

and

$$j''_l(z) = \frac{3}{4z^2} j_l(z) + \frac{j_{l+1}(z) - j_{l-1}(z)}{2z} + \frac{j_{l-2}(z) - 2j_l(z) + j_{l+2}(z)}{4} \quad (D20)$$

The recursion formula of equation (D4) for the Neumann functions was used as it was stable for the arguments and orders encountered. To speed computations

$$n'_l(z) = \frac{1}{2} \left[ n_{l-1}(z) - n_{l+1}(z) - \frac{n_l(z)}{z} \right] \quad (D21)$$

and

$$n''_l(z) = \frac{3}{4z^2} n_l(z) + \frac{n_{l+1}(z) - n_{l-1}(z)}{2z} + \frac{n_{l-2}(z) - 2n_l(z) + n_{l+2}(z)}{4} \quad (D22)$$

were used in place of equations (D5) and (D6).

## Appendix E

The integral over time in equation (53) can be evaluated as

$$\int_{-\Delta t/2}^{\Delta t/2} e^{i2\pi \left[ (f_c - f)t + \frac{(f_1 - f_0)}{2\Delta t} t^2 \right]} dt \quad (E1)$$

$$= \int_{-\Delta t/2}^{\Delta t/2} \cos \left[ \pi \frac{f_1 - f_0}{\Delta t} t^2 + 2\pi(f_c - f)t \right] dt + i \int_{-\Delta t/2}^{\Delta t/2} \sin \left[ \pi \frac{f_1 - f_0}{\Delta t} t^2 + 2\pi(f_c - f)t \right] dt \quad (E1)$$

$$= \sqrt{\frac{\Delta t}{2(f_1 - f_0)}} \left\{ \cos \left[ \frac{\pi \Delta t (f_c - f)^2}{(f_1 - f_0)} \right] C \left[ \sqrt{\frac{2\Delta t}{(f_1 - f_0)}} \left( \frac{(f_1 - f_0)}{\Delta t} t + (f_c - f) \right) \right] \right.$$

$$\left. + \sin \left[ \frac{\pi \Delta t (f_c - f)^2}{(f_1 - f_0)} \right] S \left[ \sqrt{\frac{2\Delta t}{(f_1 - f_0)}} \left( \frac{(f_1 - f_0)}{\Delta t} t + (f_c - f) \right) \right] \right\}_{-\Delta t/2}^{\Delta t/2} \quad (E2)$$

$$+ i \sqrt{\frac{\Delta t}{2(f_1 - f_0)}} \left\{ \cos \left[ \frac{\pi \Delta t (f_c - f)^2}{(f_1 - f_0)} \right] S \left[ \sqrt{\frac{2\Delta t}{(f_1 - f_0)}} \left( \frac{(f_1 - f_0)}{\Delta t} t + (f_c - f) \right) \right] \right.$$

$$\left. - \sin \left[ \frac{\pi \Delta t (f_c - f)^2}{(f_1 - f_0)} \right] C \left[ \sqrt{\frac{2\Delta t}{(f_1 - f_0)}} \left( \frac{(f_1 - f_0)}{\Delta t} t + (f_c - f) \right) \right] \right\}_{-\Delta t/2}^{\Delta t/2} \quad (E2)$$

$$= \sqrt{\frac{\Delta t}{2(f_1 - f_0)}} \exp \left[ \frac{-i\pi \Delta t (f_c - f)^2}{(f_1 - f_0)} \right] \left\{ C \left[ \sqrt{\frac{2\Delta t}{(f_1 - f_0)}} \left( \frac{(f_1 - f_0)}{\Delta t} t + (f_c - f) \right) \right] \right.$$

$$\left. + i S \left[ \sqrt{\frac{2\Delta t}{(f_1 - f_0)}} \left( \frac{(f_1 - f_0)}{\Delta t} t + (f_c - f) \right) \right] \right\}_{-\Delta t/2}^{\Delta t/2} \quad (E3)$$

$$= \sqrt{\frac{\Delta t}{2(f_1 - f_0)}} \exp \left[ \frac{-i\pi \Delta t (f_c - f)^2}{(f_1 - f_0)} \right] \left\{ \frac{1+i}{2} \operatorname{erf} \left[ \frac{\sqrt{\pi}}{2} (1-i) \sqrt{\frac{2\Delta t}{f_1 - f_0}} \left( \frac{(f_1 - f_0)}{\Delta t} t + f_c - f \right) \right] \right\}_{-\Delta t/2}^{\Delta t/2} \quad (E4)$$

where C and S are the Fresnel integrals

$$C(z) = \int_0^z \cos\left(\frac{\pi}{2}t^2\right) dt \quad (E5)$$

and

$$S(z) = \int_0^z \sin\left(\frac{\pi}{2}t^2\right) dt \quad (E6)$$

and erf is the error function

$$\operatorname{erf} z = \frac{2}{\sqrt{\pi}} \int_0^z e^{-t^2} dt \quad (E7)$$

Calculations of the Sound Scattering from Fluid-Filled Spherical  
Shell Sonar Targets

Mark Readhead

(DSTO-RR-0020)

DISTRIBUTION LIST

Director, AMRL

Chief, Maritime Operations Division

B.F. Wild

Mark Readhead

25 copies

Library, AMRL Maribyrnong

Library, AMRL Fishermens Bend

Chief Defence Scientist (for CDS, FASSP, ASSCM)

1 copy

Director, ESRL

Head, Information Centre, Defence Intelligence Organisation

OIC Technical Reports Centre, Defence Central Library

Officer in Charge, Document Exchange Centre

8 copies

Air Force Scientific Adviser, Russell Offices

Scientific Adviser - Policy and Command

Senior Librarian, Main Library DSTOS

Senior Defence Scientific Adviser

Librarian - AMRL Sydney

2 copies

Librarian, DSD, Kingston ACT

Librarian, Australian Defence Force Academy

Serials Section (M List), Deakin University Library, Deakin University, Geelong 3217

NAPOC QWG Engineer NBCD c/- DENGRS-A, HQ Engineer Centre, Liverpool

Military Area, NSW 2174

ABCRA, Russell Offices, Canberra ACT 2600

4 copies

Head of Staff, British Defence Research and Supply Staff (Australia)

NASA Senior Scientific Representative in Australia

INSPEC: Acquisitions Section Institution of Electrical Engineers

Head Librarian, Australian Nuclear Science and Technology Organisation

Senior Librarian, Hargrave Library, Monash University

Library - Exchange Desk, National Institute of Standards and Technology, US

Acquisition Unit (DSC-EO/GO), British Library, Boston Spa, Wetherby Yorkshire LS23 7BQ, England

Library, Chemical Abstracts Reference Service

Engineering Societies Library, US

Documents Librarian, The Center for Research Libraries, US

Army Scientific Adviser, Russell Offices - data sheet only

Navy Scientific Adviser

DASD, APW2-1-OA2, Anzac Park West, Canberra ACT

Director General Force Development (Land) - data sheet only

SO (Science), HQ 1 Division, Milpo, Enoggera, Qld 4057 - data sheet only

Counsellor, Defence Science, Embassy of Australia - data sheet only

Counsellor, Defence Science, Australian High Commission - data sheet only

Scientific Adviser to DSTC Malaysia, c/- Defence Adviser - data sheet only

Scientific Adviser to MRDC Thailand, c/- Defence Attaché - data sheet only

DISTRIBUTION LIST (Contd)

Mr Jim Thompson, MOD Sydney

Dr Stuart Anstee, MOD Sydney

Dr David Blair, MOD Sydney

Dr Ian Jones, MOD Sydney

Dr Ranjit Thuraisingham, MOD Sydney

Dr Don Richardson, MOD Melbourne

Dr Kurt Benke, MOD Melbourne

Dr Roger Neill, MOD Melbourne

Mr Paris Constantine, Thomson Sintra Pacific, 18/112 Talavera Rd, North Ryde NSW 2113

Dr Andrew Madry, Thomson Sintra Pacific, 18/112 Talavera Rd, North Ryde NSW 2113

Mr Ashley Deacon, GEC Marconi Systems, Faraday Park Railway Rd, Meadowbank NSW 2114

DNCSE, CP1-6-25, Campbell Park Offices, Canberra ACT 2600

MHIPD, Dept. of Defence, GP2-3-10, Campbell Park Offices, Canberra ACT 2600

MHCPD, Dept. of Defence, CP2-3-11, Campbell Park Offices, Canberra ACT 2600

MWSCPD, Dept. of Defence, CP2-2-19, Campbell Park Offices, Canberra ACT 2600

Commanding Officer, HMAS Waterhen, Halls Head Rd, Waverton NSW 2060

2 copies

REPORT NO.  
DSTO-RR-0020AR NO.  
AR-008-995REPORT SECURITY CLASSIFICATION  
UNCLASSIFIED

## TITLE

Calculations of the sound scattering from fluid-filled spherical shell sonar targets

AUTHOR(S)  
Mark ReadheadCORPORATE AUTHOR  
DSTO Aeronautical and Maritime Research Laboratory  
PO Box 4331  
Melbourne Victoria 3001REPORT DATE  
January 1995TASK NO.  
M40171SPONSOR  
MHCPDFILE NO.  
510/207/0104REFERENCES  
21PAGES  
88

CLASSIFICATION/LIMITATION REVIEW DATE

CLASSIFICATION/RELEASE AUTHORITY  
Chief, Maritime Operations Division

## SECONDARY DISTRIBUTION

Approved for public release

## ANNOUNCEMENT

Announcement of this report is unlimited

## KEYWORDS

Sound Scattering  
Sonar  
CalibratingBinary Chemical Agents  
Spherical Shell  
Sonar Transmission (Pulsed)Sonar Targets  
Sound Pressure  
Acoustic Measurement

## ABSTRACT

The theory of the sound pressure scattered from a fluid-filled spherical shell immersed in a second fluid is developed. An arbitrary combination of fluids may be used to fill the shell, and both the sound source and the receiver may be in the near field. The theory is used to calculate the pressure field in both the interior and exterior fluids and is extended to determine the time-dependence of the reflected signal and the target strength. The dependence of these quantities as a function of frequency and pulse type; shell material, diameter and wall thickness; fluid combination; temperature; and distance of the receiver from the sphere is examined, and is shown to be sensitive to most of these parameters. The performance of spheres filled with a Freon-113™ - ethanol or Fluorinert FC-72™ - n-hexane mixture is considered.